An Adaptive Directional Haar Framelet-based Reconstruction Algorithm for Parallel Magnetic Resonance Imaging

Yan-Ran Li[*]   Raymond H. Chan[†]   Lixin Shen[‡]   Yung-Chin Hsu

Wen-Yih Isaac Tseng[§]

February 1, 2016

Abstract

Parallel magnetic resonance imaging (pMRI) is a technique to accelerate the magnetic resonance imaging process. The problem of reconstructing an image from the collected pMRI data is ill-posed. Regularization is needed to make the problem well-posed. In this paper, we first construct a 2-dimensional tight framelet system whose filters have the same support as the orthogonal Haar filters and are able to detect edges of an image in the horizontal, vertical, and $\pm 45^o$ directions. This system is referred to as directional Haar framelet (DHF). We then propose a pMRI reconstruction model whose regularization term is formed by the DHF. This model is solved by a fast proximal algorithm with low computational complexity. The regularization parameters are updated adaptively and determined automatically during the iteration of the algorithm. Numerical experiments for in-silico and in-vivo data sets are provided to demonstrate the superiority of the DHF-based model and the efficiency of our proposed algorithm for pMRI reconstruction.

1   Introduction

Magnetic resonance imaging (MRI) is a non-invasive medical imaging technique used in radiology to investigate the anatomy and physiology in the human body, in both health and disease. It visualizes the internal body structure of the patients without exposing them to ionizing radiation [35]. It produces high-resolution images that can help to diagnose a variety of medical problems. However, MRI is a relatively slow imaging technique that has limited its application to imaging of time-varying objects. Patients are discomforted by the lengthy imaging procedures due to lying in a confined space, as well as having to hold their breath [44]. Parallel imaging techniques using an array of surface coils have been developed to acquire multiple sets of undersampled k-space data simultaneously to significantly accelerate the MRI process [14, 15]. Over the last two decades, a number of parallel imaging techniques and strategies have been produced for parallel

1

MRI (pMRI) image reconstruction from the undersampled data. The most well-known ones include sensitivity encoding (SENSE) [37] and generalized autocalibrating partially parallel acquisitions (GRAPPA) [18]. Both methods provide good results with nearly identical reconstruction quality [1].

SENSE has been made commercially available for clinical purposes. Many clinical applications already benefit from the capabilities of SENSE in terms of increased imaging speed, effectively reduced blurring, and increased spatial resolution provided by pMRI [44, 17]. For pMRI reconstruction by SENSE, accurate estimation of coil sensitivity is required, but it is difficult to be determined because of the complex geometry of the coils and the noise in the coil images. As a consequence, the reconstructed image by SENSE often suffers from artifacts like noise amplification [42], Gibbs effect [48] and aliasing [1]. To overcome these problems, regularization techniques that do not need modifications in hardware or data acquisition, are widely adopted for SENSE-based reconstruction model. In [31], Tikhonov regularization was used due to the existence of a closed-form solution while the regularization parameter was set automatically by using the L-curve method. With Tikhonov regularization, bias is often introduced due to the poor quality of reconstruction image, in particular, at high reduction factors.

Recently, the smooth prior used in Tikhonov regularization was replaced by non-smooth edge-preserving prior. The resulting edge-preserving regularization, like total-variation (TV) regularization [2, 46, 23] or wavelet-based regularization [8], has been proposed for pMRI reconstruction problem. In a comparison with Tikhonov regularization, edge-preserving regularization makes a noticeable improvement in preserving sharp edges of reconstructed images and removing the noise or artifacts. The accuracy of sensitivity maps is crucial for pMRI reconstruction since the aliasing artifacts, caused by inaccurate sensitivity maps, can hardly be reduced by any kind of reconstruction methods. Hence, sensitivity estimation method is as important as the reconstruction method in SENSE. In [47], a method that jointly estimates the sensitivities and SENSE reconstruction was proposed to refine the sensitivities iteratively so that the SNR of reconstruction is improved and the image artifact is reduced. In [24], a framework that allows the integration of a-priori information, such as a TV or total generalized variation penalty [3], in an iteratively regularized Gauss-Newton method, was proposed with a goal of joint estimation of images and coil sensitivities. The selection of a regularization parameter in regularization method is critical in order to achieve a reconstructed image with acceptable quality. The regularization parameter in [2, 46, 23, 8] was not set automatically; therefore, limiting their practical applications for the pMRI reconstruction.

GRAPPA [18] is a k-space method that interpolates the missing data in the k-space for each coil. It does not need to explicitly know the coil sensitivities, but requires to estimate an interpolation kernel using the auto calibration signal (ACS) data. To acquire the correct interpolation kernel for reconstructing high quality MRI images, the authors in [50, 36] regularize the GRAPPA-based interpolation kernel and estimate it by an iterative scheme. The method in [45] applies sparsity-promoting regularizers on the GRAPPA-based calibration kernel and the coil image in each channel. It jointly updates the kernel and the images iteratively.

The relationship between SENSE and GRAPPA was clarified and the gap between them was bridged in [43]. Both approaches restrict the solution to a subspace spanned by the sensitivities. By combining the advantages from both SENSE and GRAPPA, a hybrid reconstruction method to pMRI was then proposed.

Recently, compressive sensing (CS) has been applied to pMRI problems in order to accelerate imaging speed and to improve the quality of MRI images [33]. The ℓ_1-SPIRiT [34] is an algorithm for auto calibrating parallel imaging and permits an efficient implementation with clinically-feasible runtimes by using compressive sensing. The state-of-the-art ℓ_1-ESPIRiT algorithm proposed in [43] uses the wavelet regularization and sensitivities estimated from the calibration matrix as in GRAPPA. Sparse dictionary learning with compressive sensing was proposed in [38] to reconstruct MR images from highly undersampled k-space data.

This work complements the existing TV and wavelet-based regularization methods for pMRI reconstruction. The main contributions of the work are described as follows:

2

- We construct a tight framelet system based on the two-dimensional orthogonal Haar wavelet. The filters associated with this system have the same support as the filters of the orthogonal Haar wavelet and provide information of edges for an image in the horizontal, vertical, and $\pm 45^o$ directions. We call our constructed system the directional Haar framelet (DHF) system and the corresponding filters as the DHF filters. We show that the computational complexity of the DHF system is even lower than that of the classical orthogonal Haar wavelet system.

- We propose a new regularization technique that assimilates the advantages of both total variation and wavelet regularization for SENSE and remedies their drawbacks. This regularization term is the composition of a sparsity-prompting function with a weighted coefficient vector. The coefficient vector is obtained by applying the DHF filters to the underlying image. The sparsity-prompting function can simply be the ℓ_1 norm or the joint ℓ_1 norm [34], but not limited to these. We solve the proposed DHF-based pMRI reconstruction model by a fast proximal algorithm. We further develop a strategy to adaptively update and determine the regularization parameters during the iterations of the algorithm.

- We conduct experiments on in-silico and in-vivo data. Experimental results show the robustness of our DHF-based pMRI reconstruction model against the noise on different MRI machines with different coil receivers. They also show that our method requires the least CPU times to produce the best reconstructed images.

The outline of the paper is as follows. The principle of parallel MRI and particularly the SENSE-based method are reviewed in Section 2. Section 3 presents a directional Haar wavelet-based tight frame system constructed from the 2-dimensional orthogonal Haar wavelet system. We also present a sparsity-promoting regularization optimization model in real domain. A fast proximal algorithm for the proposed model is presented in Section 4. We give the reconstruction results, based on both simulation and real MRI images, in Section 5. Conclusions are given in Section 6.

2 Brief Review on SENSE-based Methods

A good MRI image can be obtained from sufficient number of samples in the k-space at the expense of long acquisition times. Fast imaging methods are required to reduce acquisition times. Recent development of parallel MRI (pMRI) is the greatest progress in increasing imaging speed. Most pMRI scanners involve skipping k-space data in the phase-encoding direction. To reduce the imaging time by a factor of $\mathfrak{r}$ (known as the *reduction factor* or the *acceleration factor*), the usual setting for pMRI is to perform k-space sampling where a downsampling factor $\mathfrak{r}$ is taken in the phase-encoding direction [1].

To recover the skipped k-space data, the receiver coils in an array of receiver surface coils are used to receive MRI signals simultaneously, and the obtained images are called the *coil images*. The receiver coils have distinct coil sensitivities depending on their positions. Hence the resulting MRI signals contain not only frequency information, but also some spatial information. Thus pMRI reconstruction algorithms can utilize this spatial information to recover the information loss due to the skipping of data. Sampling partial k-space data leads to aliasing artifacts in coil images and the sensitivity profiles of all coils help to solve the nonlinear reconstruction problem. To remove artifacts and retrieve high quality images, the techniques for pMRI can be mainly divided in two groups: image domain techniques such as PILS, SENSE, and Fourier domain techniques such as SMASH and GRAPPA.

SENSE is one of the most famous image domain-based methods and is currently used in clinical practice. SENSE needs pre-scanning full k-space data to obtain unaliased coil images for the estimation of coil sensitivity. The coil images are modulated by their individual coil sensitivities $\mathcal{S}_\ell$, where $\ell = 1, 2, \ldots, p$

with p being the number of the coils. The coil image from the ℓ-th coil is modeled as follows:

$$g_\ell = \mathcal{F}^{-1}\mathcal{P}\mathcal{F}\mathcal{S}_\ell u + \eta_\ell, \tag{1}$$

where u is the desired image, η_ℓ is the white Gaussian noise, $\mathcal{F}$ is the discrete Fourier transform matrix with inverse $\mathcal{F}^{-1}$, and $\mathcal{P}$, called sampling matrix, is a diagonal matrix with 0 and 1 (indicating the corresponding k-space data is skipped or not) at its diagonal elements [15]. The range of g_ℓ in (1) varies from coil to coil and depends on the setting of the MRI machine. Combining equations from all p coils, the set of equations in (1) can be transformed into matrix form:

$$g = Mu + \eta, \tag{2}$$

where g is all the aliased images in vector form, u is the image to be reconstructed, η represents the noise in the vector g and M is the composition of $\mathcal{F}$, its inverse, $\mathcal{P}$ and $\mathcal{S}_\ell$. More precisely,

$$g := \begin{bmatrix} g_1 \\ \vdots \\ g_p \end{bmatrix}, \quad M := \begin{bmatrix} \mathcal{F}^{-1}\mathcal{P}\mathcal{F}\mathcal{S}_1 \\ \vdots \\ \mathcal{F}^{-1}\mathcal{P}\mathcal{F}\mathcal{S}_p \end{bmatrix}, \quad \eta := \begin{bmatrix} \eta_1 \\ \vdots \\ \eta_p \end{bmatrix}. \tag{3}$$

A least squares technique is used by SENSE to reconstruct an image for model (2). Due to the complex geometry of the receiver coils, the actual sensitivities $\mathcal{S}_\ell$ are hardly possible to be pre-estimated accurately in real applications, especially in areas having low photon densities or constant blood flow [16]. These kind of errors together with noise contained in the coil images could be amplified in the reconstructed image, and resulting in severely aliasing artifacts, especially in the case with a large reduction factor. To reduce the artifacts and preserve sharp edges in the reconstructed image, the total variation regularization together with the least squares fitting was proposed to unfold the aliased images in pMRI [46, 23]. This model is formulated as

$$\min_u \left\{ \frac{1}{2}\|Mu - g\|_2^2 + \lambda\|u\|_{\mathrm{TV}} \right\}, \tag{4}$$

where $\|u\|_{\mathrm{TV}}$ is the total variation of u and λ is a positive number balancing the least squares fitting term and the total variation regularization term. The robustness of the total variation regularization against the noise and error in the estimation of the coil sensitivities was numerically confirmed in [46, 23]. However, it is well known that staircase artifacts may appear in the reconstructed image due to the total variation regularization [13], and the regularization parameter λ needs to be set individually for each MRI reconstruction problem. It was shown in [32] that Bregman iteration algorithm for problem (4) can preserve both sharp edges lost in Tikhonov regularization and fine structures missed in total variation regularization, while reducing noise and aliasing artifacts. Wavelet transforms, which enables a good space and frequency localization of useful information, have also been used in MRI reconstruction. Artifacts appeared in the basic SENSE reconstruction can be easily detected by wavelets and hence be attenuated [8]. The model formulated in the wavelet domain in [8] emphasizes the sparse representation of the underlying image, and hence edges in the reconstructed image will be enhanced. However ringing artifacts will be introduced in the reconstructed image as well due to the modification of wavelet coefficients.

3 Adaptive Directional Haar Wavelet-based Regularization Model

In this paper, the pMRI reconstruction problem (2) is solved by a new regularization model that assimilates the advantages of both total variation and wavelet regularization for SENSE and remedies their drawbacks. Our proposed optimization model for the pMRI reconstruction problem (2) is given in the form

$$\min_u \left\{ \frac{1}{2}\|Mu - g\|_2^2 + \|\Gamma W u\|_1 \right\}, \tag{5}$$

where Γ is a diagonal matrix with non-negative diagonal elements, and W is a tight frame matrix that will be constructed later. We remark that the same reconstruction model with W generated by the Haar wavelet has been used in [49] for spectral breast CT reconstruction.

In total-variational based model (4) there is a global regularization parameter λ. In contrast, for our model (5), each tight frame coefficient has its own regularization parameter. The diagonal elements of the diagonal matrix Γ are formed from these regularization parameters. By using a different regularization parameter for each coefficient, our optimization model has an ability to access the local information of the underlying image. A procedure of adaptively selecting these parameters will be given in the next section.

The mathematical model (1) is ill-posed and requires regularization techniques to make it well-posed. The total variation regularization is known to be edge-preserving and performs well especially for piecewise smooth images, but it may result in the loss of texture and may introduce staircase artifacts that are particularly visible in the vicinity of both non-horizontal and non-vertical edges. Wavelet regularization promotes the sparsity of images in wavelet domain, and hence, leads to reconstructed images with sharp edges, but also likely with ringing artifacts. The presence of artifacts by total variation regularization or wavelet regularization makes the pMRI reconstruction inefficient. Therefore, one needs to find a proper regularization to suppress these artifacts in pMRI reconstructions. One way to avoid or suppress ringing artifacts arising from wavelet regularization is to choose a wavelet system whose wavelet filters have a short support (see, e.g., [41, pages 342, 365]). The filters associated with the classical 2-dimension orthogonal Haar wavelet indeed have a short support which is $\{0, 1\}^2$. But, as it is well-known, the regularization with the orthogonal Haar wavelet is similar to the total variation regularization; therefore, staircase artifacts will appear in the neighbors of edges that are neither vertical or horizontal.

For pMRI reconstruction in (5), we will construct a tight frame matrix W that is an extension of the classical 2-dimension orthogonal Haar wavelet. Not only the support of its filters is the same as that of the 2-dimension orthogonal Haar wavelet, but it also can detect edges in the vertical, horizontal as well as $\pm 45^o$ directions. It is expected that artifacts around the edges in the vicinity of $\pm 45^o$ in the reconstructions using the orthogonal Haar wavelet can be better suppressed in the reconstructions using our constructed frame matrix W.

The rest of this section will be devoted to the construction of this matrix W. We start with an overview of tight frames. Then, we construct our directional tight Haar wavelet frame (DHF) from the well-known orthogonal Haar wavelet. Finally, we present fast DHF transform and its computational complexity. The associated matrix representation of the transform will be considered as W in (5).

3.1 Preliminaries of Tight Frames

Since the images of interest in this paper are in the two-dimensional space, we focus on tight wavelet frames on $\mathbb{R}^2$. Tight wavelet frames have been proven to be useful in image processing, see, e.g., [5, 7, 6, 9, 10, 12, 11, 28, 29, 30, 39] and the references therein.

A countable set $X \subset L^2(\mathbb{R}^2)$ is called a tight frame of $L^2(\mathbb{R}^2)$ if $f = \sum_{\mu \in X} \langle f, \mu \rangle \mu$ holds for all $f \in L^2(\mathbb{R}^2)$. Clearly, a tight frame generalizes an orthogonal basis. Comparing with an orthogonal basis, a tight frame is an overcomplete system but keeps the energy-preserving property of an orthonormal basis. For a given $\Psi := \{\psi_1, \ldots, \psi_L\} \subset L^2(\mathbb{R}^2)$, we define a system $X(\Psi)$ generated by Ψ as $X(\Psi) := \{2^n \psi_\ell(2^n \cdot -\mathbf{k}) : 1 \leq \ell \leq L, ; n \in \mathbb{Z}, \mathbf{k} \in \mathbb{Z}^2\}$. When $X(\Psi)$ forms a tight frame of $L^2(\mathbb{R}^2)$, the system $X(\Psi)$ is called a tight wavelet frame system and each function $\psi_\ell, \ell = 1, \ldots, L$, is called a tight framelet. The construction of framelets Ψ is usually based on a multiresolution analysis that is generated by some refinable function φ with refinement mask τ_0 satisfying $\varphi = 4 \sum_{\mathbf{k} \in \mathbb{Z}^2} \tau_0[\mathbf{k}] \varphi(2 \cdot -\mathbf{k})$. The construction of the framelets Ψ is reduced to finding a finite sequence of masks τ_ℓ such that

$$\psi_\ell = 4 \sum_{\mathbf{k} \in \mathbb{Z}^2} \tau_\ell[\mathbf{k}] \varphi(2 \cdot -\mathbf{k}), \tag{6}$$

for $1 \leq \ell \leq L$. The set $\{\tau_\ell : 0 \leq \ell \leq L\}$ is called a frame filter bank, τ_ℓ, $1 \leq \ell \leq L$ are called wavelet frame masks or the highpass filters of the system, and the refinement mask τ_0 is known as the lowpass filter. By unitary extension principle, as long as the masks τ_ℓ, $1 \leq \ell \leq L$, are finitely supported and their Fourier series $\widehat{\tau}_\ell$ satisfy

$$\sum_{\ell=0}^{L} \widehat{\tau}_\ell(\omega)\overline{\widehat{\tau}_\ell(\omega + \nu)} = \begin{cases} 1, & \text{if } \nu = (0,0); \\ 0, & \text{if } \nu \in \{0, \pi\}^2 \backslash \{(0,0)\} \end{cases} \tag{7}$$

for all $\omega \in [-\pi, \pi]^2$, $X(\Psi)$ with $\Psi = \{\psi_1, \ldots, \psi_L\}$ given by (6) forms a tight wavelet frame of $L^2(\mathbb{R}^2)$. Recall that for a mask a, $\widehat{a}(\omega) := \sum_{\mathbf{k} \in \mathbb{Z}^2} a[\mathbf{k}]e^{-\imath \mathbf{k} \cdot \omega}$ which is a 2π-periodic function. Here, and in the sequel, $\imath$ denotes the imaginary unit.

3.2 Directional Tight Haar Wavelet Frame (DHF)

Our directional tight Haar wavelet frame (DHF) is constructed via orthogonal Haar wavelet. Recall that the 2-dimensional orthogonal Haar wavelet filters are

$$h_0[\mathbf{k}] = \begin{cases} \frac{1}{4}, & \text{if } \mathbf{k} \in \{0,1\}^2; \\ 0, & \text{otherwise}, \end{cases} \quad h_1[\mathbf{k}] = \begin{cases} \frac{1}{4}, & \text{if } \mathbf{k} = (0,0) \text{ or } (1,0); \\ -\frac{1}{4}, & \text{if } \mathbf{k} = (0,1) \text{ or } (1,1); \\ 0, & \text{otherwise}, \end{cases}$$

$$h_2[\mathbf{k}] = \begin{cases} \frac{1}{4}, & \text{if } \mathbf{k} = (0,0) \text{ or } (0,1); \\ -\frac{1}{4}, & \text{if } \mathbf{k} = (1,0) \text{ or } (1,1); \\ 0, & \text{otherwise}, \end{cases} \quad h_3[\mathbf{k}] = \begin{cases} \frac{1}{4}, & \text{if } \mathbf{k} = (0,0) \text{ or } (1,1); \\ -\frac{1}{4}, & \text{if } \mathbf{k} = (0,1) \text{ or } (1,0); \\ 0, & \text{otherwise}. \end{cases}$$

It can be directly verified that $\sum_{\ell=0}^{3} |\widehat{h}_\ell(\omega)|^2 = 1$ and $\sum_{\ell=0}^{3} \widehat{h}_\ell(\omega)\overline{\widehat{h}_\ell(\omega + \nu)} = 0$ for $\nu \in \{0, \pi\}^2 \backslash \{(0,0)\}$. The scaling function $\varphi(x, y)$ equals 1 for $(x, y) \in [0,1]^2$ and 0 otherwise. Three wavelets corresponding to the highpass filters h_1, h_2 and h_3 at $(x, y) \in \mathbb{R}^2$ are

$$\psi_1(x, y) = \begin{cases} 1, & \text{if } (x, y) \in [0,1] \times [0, 1/2); \\ -1, & \text{if } (x, y) \in [0,1] \times [1/2, 1]; \\ 0, & \text{otherwise}, \end{cases}$$

$\psi_2(x, y) = \psi_1(y, x)$, and $\psi_3(x, y) = \psi_1(x, y)\psi_2(x, y)$, respectively.

With the orthogonal Haar wavelet filters h_ℓ, we define the masks τ_ℓ, $0 \leq \ell \leq 6$, as follows

$$\begin{bmatrix} \widehat{\tau}_0(\omega) \\ \widehat{\tau}_1(\omega) \\ \widehat{\tau}_2(\omega) \\ \widehat{\tau}_3(\omega) \\ \widehat{\tau}_4(\omega) \\ \widehat{\tau}_5(\omega) \\ \widehat{\tau}_6(\omega) \end{bmatrix} = \begin{bmatrix} 1 & 0 & 0 & 0 \\ 0 & \frac{1}{2} & \frac{1}{2} & 0 \\ 0 & \frac{1}{2} & \frac{-1}{2} & 0 \\ 0 & \frac{1}{2} & 0 & \frac{1}{2} \\ 0 & 0 & \frac{1}{2} & \frac{1}{2} \\ 0 & \frac{1}{2} & 0 & \frac{-1}{2} \\ 0 & 0 & \frac{1}{2} & \frac{-1}{2} \end{bmatrix} \begin{bmatrix} \widehat{h}_0(\omega) \\ \widehat{h}_1(\omega) \\ \widehat{h}_2(\omega) \\ \widehat{h}_3(\omega) \end{bmatrix}. \tag{8}$$

It can be shown directly that the masks τ_ℓ given in (8) satisfy (7) with $L = 6$; therefore, they form a 2-dimensional tight frame filter bank. In this filter bank, the refinement mask τ_0 is the same as h_0 while the six wavelet frame masks τ_1, τ_2, τ_3, τ_4, τ_5, and τ_6 are, respectively,

$$\tau_1[\mathbf{k}] = \begin{cases} \frac{1}{4}, & \text{if } \mathbf{k} = (0,0); \\ -\frac{1}{4}, & \text{if } \mathbf{k} = (1,1); \\ 0, & \text{otherwise}, \end{cases} \quad \tau_2[\mathbf{k}] = \begin{cases} \frac{1}{4}, & \text{if } \mathbf{k} = (1,0); \\ -\frac{1}{4}, & \text{if } \mathbf{k} = (0,1); \\ 0, & \text{otherwise}, \end{cases} \quad \tau_3[\mathbf{k}] = \begin{cases} \frac{1}{4}, & \text{if } \mathbf{k} = (0,0); \\ -\frac{1}{4}, & \text{if } \mathbf{k} = (0,1); \\ 0, & \text{otherwise}, \end{cases}$$

$$\tau_4[\mathbf{k}] = \begin{cases} \frac{1}{4}, & \text{if } \mathbf{k} = (0,0); \\ -\frac{1}{4}, & \text{if } \mathbf{k} = (1,0); \\ 0, & \text{otherwise}, \end{cases} \quad \tau_5[\mathbf{k}] = \begin{cases} \frac{1}{4}, & \text{if } \mathbf{k} = (1,0); \\ -\frac{1}{4}, & \text{if } \mathbf{k} = (1,1); \\ 0, & \text{otherwise}, \end{cases} \quad \tau_6[\mathbf{k}] = \begin{cases} \frac{1}{4}, & \text{if } \mathbf{k} = (0,1); \\ -\frac{1}{4}, & \text{if } \mathbf{k} = (1,1); \\ 0, & \text{otherwise}, \end{cases} \tag{9}$$

These wavelet frame filters acting as difference operators have an ability to provide directional information of an image when they are applied onto the image. More precisely, the filters τ_1 and τ_2 act as the first-order difference operator in the 45° and 135° directions, respectively. Both τ_3 and τ_5 are the first-order difference operator in the horizontal direction while both τ_4 and τ_6 are the first-order difference operator in the vertical direction. For easy exposition in the later discussion, our constructed wavelet frame filters are refereed to as the DHF filters.

For the tight frame system associated with the DHF filter, the corresponding scaling function φ is exactly the same as the scaling function of the orthogonal Haar wavelet system. Through (6) and (9), one can get directly that the tight framelets $\psi_1, \psi_3, \psi_2, \psi_4, \psi_5,$ and ψ_6 corresponding $\tau_1, \tau_3, \tau_2, \tau_4, \tau_5,$ and τ_6 at $(x, y) \in \mathbb{R}^2$ are

$$\psi_1(x,y) = \begin{cases} 1, & \text{if } (x,y) \in [0,1/2) \times [0,1/2); \\ -1, & \text{if } (x,y) \in [1/2,1] \times [1/2,1]; \\ 0, & \text{otherwise,} \end{cases} \qquad \psi_3(x,y) = \begin{cases} 1, & \text{if } (x,y) \in [0,1/2) \times [0,1/2); \\ -1, & \text{if } (x,y) \in [0,1/2) \times [1/2,1]; \\ 0, & \text{otherwise,} \end{cases}$$

$\psi_2(x,y) = \psi_1(y, 1-x)$, $\psi_4(x,y) = \psi_3(y,x)$, $\psi_5(x,y) = \psi_3(x-1/2, y)$, and $\psi_6(x,y) = \psi_3(y-1/2, x)$, respectively. We can see that the scaling function and framelets for both the orthogonal Haar wavelet and the DHF system are supported on $[0,1]^2$.

3.3 Fast DHF Transform and Its Computational Complexity

Next we present the fast frame transform for DHF when applied onto images. To this end, for $j \geq 1$ we define

$$\tau_{j,i} := \widetilde{\tau}_{j,i} * \widetilde{\tau}_{j-1,0} * \cdots * \widetilde{\tau}_{0,0} \tag{10}$$

with $\tau_{0,i} = \tau_i$ and

$$\widetilde{\tau}_{j,i}[\mathbf{k}] = \begin{cases} \tau_i[2^{-j}\mathbf{k}], & \mathbf{k} \in 2^j\mathbb{Z}^2; \\ 0, & \mathbf{k} \notin 2^j\mathbb{Z}^2. \end{cases}$$

Here $*$ denotes the convolution operator. The relationship among the filters $\tau_{j,i}$, for $3 \leq i \leq 6$ is described as follows.

Proposition 1 *For the filters given in (10), then for all $j \geq 0$ and $\omega = (\omega_1, \omega_2) \in [-\pi, \pi]^2$,*

$$\widehat{\tau}_{j,5}(\omega) = e^{-\imath 2^j \omega_1}\widehat{\tau}_{j,3}(\omega) \quad and \quad \widehat{\tau}_{j,6}(\omega) = e^{-\imath 2^j \omega_2}\widehat{\tau}_{j,4}(\omega)$$

Moreover, $|\widehat{\tau}_{j,3}(\omega)| = |\widehat{\tau}_{j,5}(\omega)|$ and $|\widehat{\tau}_{j,4}(\omega)| = |\widehat{\tau}_{j,6}(\omega)|$.

Proof: We only need to prove $\widehat{\tau}_{j,5}(\omega) = e^{-\imath 2^j \omega_1}\widehat{\tau}_{j,3}(\omega)$, the other follows similarly.

It follows from (9) that $\widehat{\tau}_3(\omega) = \frac{1}{4} - \frac{1}{4}e^{-\imath\omega_2}$ and $\widehat{\tau}_5(\omega) = \frac{1}{4}e^{-\imath\omega_1} - \frac{1}{4}e^{-\imath(\omega_1+\omega_2)}$. Hence, $\widehat{\tau}_5(\omega) = e^{-\imath\omega_1}\widehat{\tau}_3(\omega)$, that is, $\widehat{\tau}_{0,5}(\omega) = e^{-\imath\omega_1}\widehat{\tau}_{0,3}(\omega)$. By the definition of $\widetilde{\tau}_{j,i}$, one has that $\widehat{\widetilde{\tau}}_{j,3}(\omega) = \widehat{\tau}_{0,3}(2^j\omega)$ and $\widehat{\widetilde{\tau}}_{j,5}(\omega) = \widehat{\tau}_{0,5}(2^j\omega)$. From (10), we obtain $\widehat{\tau}_{j,3}(\omega) = \widehat{\widetilde{\tau}}_{j,3}(\omega) \prod_{k=0}^{j-1}\widehat{\widetilde{\tau}}_{k,0}(\omega)$ and $\widehat{\tau}_{j,5}(\omega) = \widehat{\widetilde{\tau}}_{j,5}(\omega)\prod_{k=0}^{j-1}\widehat{\widetilde{\tau}}_{k,0}(\omega)$. Hence, $\widehat{\tau}_{j,5}(\omega) = e^{-\imath 2^j\omega_1}\widehat{\tau}_{j,3}(\omega)$ which yields $|\widehat{\tau}_{j,3}(\omega)| = |\widehat{\tau}_{j,5}(\omega)|$ immediately. $\qquad\square$

The implication of Proposition 1 in computational savings of the fast frame transform using the DHF filters will be clear soon.

Let $\mathbf{u}$ be an image of size $n_1 \times n_2$ in $\mathbb{R}^{n_1 \times n_2}$. The 2-dimensional fast frame transform using the DHF filters with levels of decomposition J for $\mathbf{u} \in \mathbb{R}^{n_1 \times n_2}$ is given by

$$\mathbf{Wu} = \{\mathbf{W}_{j,i}\mathbf{u} : 0 \leq j \leq J-1, 0 \leq i \leq 6\}, \tag{11}$$

7

where $\mathbf{W}_{j,i}\mathbf{u} := \tau_{j,i}[-\cdot] \circledast \mathbf{u} \in \mathbb{R}^{n_1 \times n_2}$ with $\circledast$ being the convolution operator under a proper boundary condition, such as periodic or symmetric boundary. We observe that the frame transform generates more data at the output than at the input. The redundancy rate is the ratio of the number of components in the output to that in the input. Clearly, the redundancy rate depends on the number of filters as well as the number of levels in decomposition. At first glance, for single level decomposition, the redundancy rate of the DHF system is 7 while the redundancy rate of the Haar system is 4. However, in the following, we show that the computational complexity of DHF is actually lower than that of Haar system.

First we note that, by exploring the structures of the pairs of the filters (τ_3, τ_5) and (τ_4, τ_6), and ignoring the boundary issue, we have

$$(\mathbf{W}_{0,5}\mathbf{u})[k_1, k_2] = (\mathbf{W}_{0,3}\mathbf{u})[k_1 - 1, k_2] \quad \text{and} \quad (\mathbf{W}_{0,6}\mathbf{u})[k_1, k_2] = (\mathbf{W}_{0,4}\mathbf{u})[k_1, k_2 - 1],$$

which can be viewed as a consequence of Proposition 1 with $j = 0$. Therefore, the redundancy rate of the DHF system is about $\frac{5}{4}$ higher than that of the Haar wavelet system.

The operator $\mathbf{W}_{j,i}$ in (11) is a linear operator and we use $W_{j,i}$, an $n \times n$ matrix with $n = n_1 n_2$, to denote its matrix representation. We further form a matrix W of size $(6J + 1)n \times n$ by stacking the matrices

$$W_{J-1,0}, \underbrace{W_{J-1,1}, \ldots, W_{J-1,6}}, \underbrace{W_{J-2,1}, \ldots, W_{J-2,6}}, \ldots, \underbrace{W_{0,1}, \ldots, W_{0,6}}. \tag{12}$$

This matrix W serves as the matrix representation of the fast frame transform $\mathbf{W}$ given in (11). The identity $W^\top W = I$ holds due to (7), but $W^\top W \neq I$, where the superscript $\top$ denotes the conjugate transpose. For simplicity, we call W the DHF matrix and it will be used in problem (5).

By Proposition 1, the identities of $|\widehat{\tau}_{j,3}(\omega)| = |\widehat{\tau}_{j,5}(\omega)|$ and $|\widehat{\tau}_{j,4}(\omega)| = |\widehat{\tau}_{j,6}(\omega)|$ lead to

$$W_{j,3}^\top W_{j,3} = W_{j,5}^\top W_{j,5} \quad \text{and} \quad W_{j,4}^\top W_{j,4} = W_{j,6}^\top W_{j,6},$$

respectively, all $0 \leq j \leq J - 1$. Therefore, it would not be necessary to compute the coefficients $\mathbf{W}_{j,5}\mathbf{u}$ and $\mathbf{W}_{j,6}\mathbf{u}$ in our later applications. In this sense, although the filters τ_i, $i \in \{0, 1, 2, 3, 4\}$ cannot form a tight frame system, but they are sufficient for the decomposition and reconstruction of images. Including two additional filters τ_5 and τ_6 into the set of filters τ_i, $i \in \{0, 1, 2, 3, 4\}$ will enable us to generate a tight frame system.

By the above discussion, we conclude that the computational complexity of the fast frame transform with the DHF is even lower than that with the Haar filter. Actually, the computational cost of one level decomposition (resp. reconstruction) of an image with n pixels via the DHF needs $7n$ additions and n multiplications (resp. $13n$ additions and n multiplications). As a comparison, the computational cost of one level decomposition (resp. reconstruction) of an image with n pixels via the Haar filters needs $12n$ additions and n multiplications (resp. $15n$ additions and n multiplications).

From now on, a 2-dimensional image $\mathbf{u} \in \mathbb{R}^{n_1 \times n_2}$ will be viewed as a vector $u \in \mathbb{R}^n$ by concatenating its columns. The vector $w := Wu$ is the tight frame coefficients of u and satisfy the perfect reconstruction formula, i.e., $u = W^\top W u = W^\top w$.

4   A Fast Adaptive DHF Algorithm

In this section, we will develop algorithms for solving the optimization problem (5). First, to prepare for an efficient numerical algorithm for the optimization problem (5), a constrained optimization problem equivalent to (5) is presented. Next, we develop an iterative scheme based on proximity operator for the constrained optimization problem. Since the regularization parameter matrix Γ is involved in this problem, an adaptive scheme is developed to estimate it in each step of the iterative scheme. Finally, an algorithm stemming from the iterative scheme together with the estimation of Γ is proposed for solving the resulting optimization problem (16).

8

4.1 Constrained Optimization Problem

In the fidelity term $\|Mu - g\|_2^2$ of the optimization problem (5), the image u is a real vector while the observed image g is a complex vector since the Fourier matrix is involved in the formulation of the imaging matrix M. We now reformulate this fidelity term such that the resulting fidelity term is formed by a real matrix and vectors.

Hereafter, $\mathrm{Re}(\cdot)$ and $\mathrm{Im}(\cdot)$ stand for the real and imaginary parts, respectively. Define

$$P = \begin{bmatrix} \mathrm{Re}(M) \\ \mathrm{Im}(M) \end{bmatrix}, \quad z = \begin{bmatrix} \mathrm{Re}(g) \\ \mathrm{Im}(g) \end{bmatrix}, \quad \epsilon = \begin{bmatrix} \mathrm{Re}(\eta) \\ \mathrm{Im}(\eta) \end{bmatrix}. \tag{13}$$

With these matrices and vectors, the observed model (1) can be rephrased as

$$z = Pu + \epsilon. \tag{14}$$

For real-valued vector u, $\|Mu - g\|_2^2 = \|Pu - z\|_2^2$. As a consequence, problem (5) becomes

$$\min_u \left\{ \frac{1}{2}\|Pu - z\|_2^2 + \|\Gamma W u\|_1 \right\}. \tag{15}$$

No complex numbers and operators are involved in the above formulation. Therefore, it will facilitate the development of numerical algorithms for (15).

For problem (15), we denote by w the tight frame coefficient vector of u with the DHF matrix W, that is, $w = Wu$. This says that w is in the range of W. Since W is the tight frame matrix, from the relation $W^\top W = I$ the vector satisfies the condition $w = WW^\top w$. Hence, the optimization problem (15) is converted to

$$\begin{aligned} \text{minimize} \quad & \tfrac{1}{2}\|PW^\top w - z\|_2^2 + \|\Gamma w\|_1 \\ \text{subject to} \quad & w = WW^\top w \end{aligned} \tag{16}$$

The two optimization problems (15) and (16) are equivalent in the following sense. If $u^\star$ is a solution to problem (15), then $w^\star = Wu^\star$ is a solution to problem (16). Conversely, if $w^\star$ is a solution to problem (16), then $u^\star = W^\top w^\star$ is a solution to problem (15). An iterative scheme will be proposed to solve the optimization problem (16) in the next subsection.

4.2 A Proximity Operator Algorithm for Problem (16)

In this subsection, we propose an iterative scheme based on the proximity operator for solving problem (16) such that each step in the scheme can be computed efficiently.

We begin by introducing our notation and recalling some necessary background from convex analysis. The class of all lower semicontinuous convex functions $f : \mathbb{R}^d \to (-\infty, +\infty]$ such that $\mathrm{dom}\, f := \{x \in \mathbb{R}^d : f(x) < +\infty\} \neq \emptyset$ is denoted by $\Gamma_0(\mathbb{R}^d)$. The indicator function of a closed convex set C in $\mathbb{R}^d$ is defined, at $u \in \mathbb{R}^d$, as

$$\iota_C(u) := \begin{cases} 0, & \text{if } u \in C, \\ +\infty, & \text{otherwise.} \end{cases}$$

Clearly, the indicator function ι_C is in $\Gamma_0(\mathbb{R}^d)$ for any closed nonempty convex set C. With the notion of the indicator function, the optimization problem (16) can be rewritten as

$$\min_w \left\{ \frac{1}{2}\|PW^\top w - z\|_2^2 + \|\Gamma w\|_1 + \iota_{\{0\}}((I - WW^\top)w) \right\}. \tag{17}$$

The objective function in (17) is the sum of three convex functions. We propose to apply an algorithm developed recently in [27] for problem (17). To this end, we first recall two notions, namely proximity operator and conjugate function.

For a function $f \in \Gamma_0(\mathbb{R}^d)$, the proximity operator of f with parameter λ, denoted by $\text{prox}_{\lambda f}$, is a mapping from $\mathbb{R}^d$ to itself, defined for a given point $x \in \mathbb{R}^d$ by

$$\text{prox}_{\lambda f}(x) := \text{argmin}\left\{\frac{1}{2\lambda}\|u - x\|_2^2 + f(u) : u \in \mathbb{R}^d\right\}.$$

We also need the notation of the conjugate. The conjugate of $f \in \Gamma_0(\mathbb{R}^d)$ is the function $f^* \in \Gamma_0(\mathbb{R}^d)$ defined at $x \in \mathbb{R}^d$ by $f^*(x) := \sup\{\langle u, x\rangle - f(u) : u \in \mathbb{R}^d\}$.

Theorem 1 (Theorem 5.3 in [27]) *For $f \in \Gamma_0(\mathbb{R}^m)$, $r \in \Gamma_0(\mathbb{R}^n)$, and a differentiable $h \in \Gamma_0(\mathbb{R}^m)$, consider an optimization problem of the form*

$$\min_w\{h(w) + f(w) + r(Bw)\}, \tag{18}$$

where B is an $n \times m$ real matrix. For positive numbers α and β, and $\theta \geq 0$, begin with $t^0 = 1$ and an arbitrary pair $(v^0, w^0) \in \mathbb{R}^n \times \mathbb{R}^m$, we generate a sequence $\{(v^k, w^k)\}$ with the following iterative scheme

$$\begin{cases} \widetilde{v}^{k+1} &= \text{prox}_{\beta r^*}(v^k + \beta B w^k), \\ \widetilde{w}^{k+1} &= \text{prox}_{\alpha f}(w^k - \alpha B^\top(2\widetilde{v}^{k+1} - v^k) - \alpha\nabla h(w^k)), \\ t^k &= \frac{1+\sqrt{1+4(t^{k-1})^2}}{2}, \\ \begin{bmatrix} v^{k+1} \\ w^{k+1} \end{bmatrix} &= \begin{bmatrix} v^k \\ w^k \end{bmatrix} + \left(\frac{t^{k-1}-1}{t^k} + \theta\right)\begin{bmatrix} \widetilde{v}^{k+1} - v^k \\ \widetilde{w}^{k+1} - w^k \end{bmatrix}. \end{cases} \tag{19}$$

We assume that problem (18) has a solution and the gradient of h is Lipschitz continuous with Lipschitz constant $\mathcal{L}$. If

$$\frac{1}{\alpha} - \frac{\mathcal{L}}{2} > \beta\|B\|_2^2 \quad \text{and} \quad \theta < \frac{1 + \max\{\frac{1}{2}, \frac{\mathcal{L}}{\mathcal{L}+2\rho}\}}{2\max\{\frac{1}{2}, \frac{\mathcal{L}}{\mathcal{L}+2\rho}\}} - 1,$$

where $\rho = \min\left\{\frac{1}{\alpha} - \frac{\mathcal{L}}{2}, \frac{1}{\beta}\right\} \cdot \left(1 - \|B\|_2\sqrt{\beta(\frac{1}{\alpha} - \frac{\mathcal{L}}{2})^{-1}}\right)$, then the sequence $\{w^k\}$ converges to a solution of problem (18).

We now apply Theorem 1 to the optimization problem (17) (i.e., (16)). To this end, we identify $\frac{1}{2}\|PW^\top \cdot -z\|_2^2$, $\|\cdot\|_1 \circ \Gamma$, $\iota_{\{0\}}$, and $I - WW^\top$ in the objective function of (17) as h, f, r, and B in that of (18), respectively. In this scenario, we first compute $\|I - WW^\top\|_2$.

Lemma 1 *Let W be a DHF matrix. Then $\|W\|_2 = 1$ and $\|I - WW^\top\|_2 = 1$.*

Proof: Since W is a DHF matrix, that is, $W^\top W = I$, it implied that $\|W\|_2 = 1$. Further Since $(I - WW^\top)^2 = I - WW^\top$ and $I \neq WW^\top$, then $\|I - WW^\top\|_2 = 1$. □

Next, to show the gradient of h is Lipschitz continuous, we introduce a constant related to the sensitivity matrices $\mathcal{S}_i$ as

$$\kappa := \max_k \sum_{i=1}^p |s_k^{(i)}|^2, \tag{20}$$

where $s_k^{(i)}$, the k-th diagonal element of the sensitivity matrix $\mathcal{S}_i$, is the sensitivity coefficient of the i-th coil at the k-th pixel.

Lemma 2 *Let P and z be given in (13), and let W be the DHF matrix. Define $h(w) = \frac{1}{2}\|PW^\top w - z\|_2^2$ for $w \in \mathbb{R}^m$. Then the gradient of h is κ-Lipschitz continuous, where κ is given in (20).*

Proof: A direct computation gives $\nabla h(w) = WP^\top(PW^\top w - z)$. Hence, the gradient of h is $\|PW^\top\|_2^2$-Lipschitz continuous. By Lemma 1, $\|PW^\top\|_2^2 \le \|P\|_2^2$. Now, let us estimate the norm of P. By (13) and (3), we have

$$P^\top P = \sum_{i=1}^{p} \mathcal{S}_i^\top \mathcal{F}^{-1}\mathcal{P}\mathcal{F}\mathcal{S}_i. \tag{21}$$

Hence, the $k\ell$-th entry of the matrix $\mathcal{S}_i^\top \mathcal{F}^{-1}\mathcal{P}\mathcal{F}\mathcal{S}_i$ is the corresponding entry of the matrix $\mathcal{F}^{-1}\mathcal{P}\mathcal{F}$ multiplied by $\overline{s_k^{(i)}}s_\ell^{(i)}$. Likewise, from (21), the $k\ell$-th entry of the matrix $P^\top P$ is the corresponding entry of the matrix $\mathcal{F}^{-1}\mathcal{P}\mathcal{F}$ multiplied by $\sum_{i=1}^p \overline{s_k^{(i)}}s_\ell^{(i)}$. Define a $p \times m$ matrix S whose ij-th entry is $s_j^{(i)}$ and $Q = S^\top S$. Clearly, the $k\ell$-th entry of Q is $\sum_{i=1}^p \overline{s_k^{(i)}}s_\ell^{(i)}$. Thus, equation (21) can be rewritten as

$$P^\top P = Q \diamond (\mathcal{F}^{-1}\mathcal{P}\mathcal{F}), \tag{22}$$

where $\diamond$ denotes the Hadamard product. Since the sampling matrix $\mathcal{P}$ is a diagonal matrix with 0 and 1 as its diagonal elements, then $\mathcal{F}^{-1}\mathcal{P}\mathcal{F}$ is positive semi-definite and $\|\mathcal{F}^{-1}\mathcal{P}\mathcal{F}\|_2 \le 1$. By Theorem 5.5.18 in [20], from (22) we have that

$$\|P^\top P\|_2 \le \|\mathcal{F}^{-1}\mathcal{P}\mathcal{F}\|_2 \cdot \max_k \sum_{i=1}^{p} |s_k^{(i)}|^2 \le \kappa.$$

This completes the proof. $\qquad\square$

Finally, we present the proximity operators of $\|\cdot\|_1 \circ \Gamma$ and $\iota_{\{0\}}$. To this end, we recall that for a given $p \times p$ diagonal matrix D with non-negative diagonal elements, the soft shrinkage operator with respect to the threshold matrix D is denoted by shrink_D that maps $\mathbb{R}^p$ to itself. For a vector $x \in \mathbb{R}^p$, the i-th entry of the vector $y = \mathrm{shrink}_D(x)$ is $\mathrm{sign}(x_i)\max\{|x_i| - d_{ii}, 0\}$, where x_i is the i-th entry of x and d_{ii} is the i-th diagonal entry of D.

Lemma 3 *Let Γ be an $m \times m$ diagonal matrix with nonnegative diagonal elements. Define $f(w) = \|\Gamma w\|_1$ and $r(w) = \iota_{\{0\}}(w)$ for $w \in \mathbb{R}^m$. Then for any positive numbers α and β and $w \in \mathbb{R}^m$,*

$$\mathrm{prox}_{\alpha f}(w) = \mathrm{shrink}_{\alpha\Gamma}(w) \quad and \quad \mathrm{prox}_{\beta r^*}(w) = w.$$

Proof: It is well-known that $\mathrm{prox}_{\alpha f}(w) = \mathrm{shrink}_{\alpha\Gamma}(w)$ for all $w \in \mathbb{R}^m$. We just need to show $\mathrm{prox}_{\beta r^*}(w) = w$. From the definition of conjugate function, we have that $r^*(w) = 0$. Hence,

$$\mathrm{prox}_{\beta r^*}(w) = \mathrm{argmin}\left\{\frac{1}{2\beta}\|v - x\|_2^2 : v \in \mathbb{R}^m\right\} = w$$

for all $w \in \mathbb{R}^m$. This completes the proof. $\qquad\square$

With the above preparation, the application of Theorem 1 to the optimization problem (17) is stated in the following theorem.

Theorem 2 *For positive numbers α and β, and $\theta \ge 0$, begin with $t^0 = 1$ and an arbitrary pair $(v^0, w^0) \in \mathbb{R}^n \times \mathbb{R}^m$, we generate a sequence $\{(v^k, w^k)\}$ with the following iterative scheme*

$$\begin{cases} \widetilde{w}^{k+1} &= \mathrm{shrink}_{\alpha\Gamma}(w^k - \alpha(I - WW^\top)(v^k + 2\beta w^k) - \alpha WP^\top(PW^\top w^k - z)), \\ t^k &= \frac{1+\sqrt{1+4(t^{k-1})^2}}{2}, \\ \begin{bmatrix} v^{k+1} \\ w^{k+1} \end{bmatrix} &= \begin{bmatrix} v^k \\ w^k \end{bmatrix} + \left(\frac{t^{k-1}-1}{t^k} + \theta\right)\begin{bmatrix} \beta(I - WW^\top)w^k \\ \widetilde{w}^{k+1} - w^k \end{bmatrix}. \end{cases} \tag{23}$$

If the parameters α, β and θ satisfy the following conditions

$$\frac{1}{\alpha} - \frac{\kappa}{2} > \beta \quad and \quad \theta < \frac{1 + \max\{\frac{1}{2}, \frac{\kappa}{\kappa + 2\rho}\}}{2\max\{\frac{1}{2}, \frac{\kappa}{\kappa + 2\rho}\}} - 1, \tag{24}$$

where κ is given by (20) *and $\rho = \min\left\{\frac{1}{\alpha} - \frac{\kappa}{2}, \frac{1}{\beta}\right\} \cdot \left(1 - \sqrt{\beta(\frac{1}{\alpha} - \frac{\kappa}{2})^{-1}}\right)$, then the sequence $\{w^k\}$ converges to a solution of problem* (17).

Proof: We identify $\frac{1}{2}\|PW^\top \cdot -z\|_2^2$, $\|\cdot\|_1 \circ \Gamma$, $\iota_{\{0\}}$, and $I - WW^\top$ in the objective function of (17) as h, f, r, and B in that of (18), respectively. By Lemma 3, the first equation in the iterative scheme (19) becomes $\widetilde{v}^{k+1} = v^k + \beta(I - WW^\top)w^k$. By substituting $\widetilde{v}^{k+1}$ in the second and fourth equations of (19) by $v^k + \beta(I - WW^\top)w^k$, the iterative scheme reduces to (23). By Lemmas 1 and 2 and Theorem 1, if the conditions in (24) are satisfied, then sequence $\{w^k\}$ will converge to a solution of problem (17). $\qquad\square$

4.3 Estimation of the Regularization Parameter Matrix Γ

It is well known that the performance of a regularized optimization problem relies heavily on the selection of the associated regularization parameters. However, it is still an active research area to find an efficient way to estimate these parameters. Our tight wavelet frame based optimization problem (17) (or equivalently (16)) allows us to estimate the regularization parameter matrix Γ through analyzing the statistics of frame coefficients. We now provide a detailed description of the estimation of Γ.

In the optimization problem (17), the vector w collects all tight frame coefficients of the underlying image. When the iterative scheme (23) is applied to the optimization problem (17), it can be seen from (23) that the vector $\widetilde{w}$ is the penalized version of w together with a perturbation with respect to the thresholding matrix $\alpha\Gamma$. From the definition of the shrinkage operator, the value of each entry in $\widetilde{w}$ is determined by the corresponding threshold in Γ and the value of the corresponding entry in w. Intuitively, an entry with a large magnitude in w encodes edge information at a related location in the underlying image and should be kept or less affected; therefore, a small threshold should be used. On the other hand, an entry with a small magnitude in w is likely killed by a large threshold. In a nutshell, the regularization parameter matrix Γ should adapt to the geometric information of the image and the statistical modeling of the frame coefficients. Following our work in [29], we propose the following way to find Γ.

Suppose that the matrix $W \in \mathbb{R}^{m \times q}$ is formed from the fast DHF transform with J decomposition levels and $w \in \mathbb{R}^m$ is the coefficient vector obtained by applying W to the underlying image. For the i-th entry of w, there is an unique index $(\ell, j, \mathbf{k})$ with $1 \leq \ell \leq J$, $0 \leq j \leq 6$, and $\mathbf{k} \in \mathbb{Z}^2$, denoted by $\mathcal{I}(i)$, associated with i. If $\mathcal{I}(i) = (\ell, j, \mathbf{k})$, it says that w_i is the coefficient at the $\mathbf{k}$ location of a matrix and in the j-th sub-band at the ℓ-th level of decomposition. Then, the i-th diagonal entry of Γ is estimated as follows (see, [29]):

$$\gamma_i = \begin{cases} 0, & \text{if } (\ell, j) = (J, 0), \\ \frac{\sqrt{2}\sigma_{\ell,j}^2}{\sigma_{\mathcal{I}(i)}}, & \text{otherwise,} \end{cases} \tag{25}$$

where $\mathcal{I}(i) = (\ell, j, \mathbf{k})$. Here, $\sigma_{\ell,j}^2$ is the noise variance of the coefficients in the j-th subband at the ℓ-th decomposition level while $\sigma_{\mathcal{I}(i)}^2$ is the variance of w_i with the assumption that this coefficient is Laplace distributed. In practice, we suppose the noise has an independent, identically distributed Gaussian distribution, and estimate the noise variance on the image $W^\top w$ by the method in [22]. The noise variance $\sigma_{\ell,j}^2$ of the coefficients at each subband is computed as our prior method in [28] while $\sigma_{\mathcal{I}(i)}^2$ is approximatively

estimated by (see [21])

$$\sigma_{\mathcal{I}(i)}^2 = \max \left\{ \left[\frac{1.25\sqrt{2}}{|\mathfrak{W}(\mathcal{I}(i))|} \sum_{\mathbf{k} \in \mathfrak{W}(\mathcal{I}(i))} |w_{\mathbf{k}}| \right]^2 - \sigma_{\ell,j}^2, 10^{-9} \right\},$$

where the set $\mathfrak{W}(\mathcal{I}(i))$ contains all indexes of coefficients in the neighborhood of the coefficient w_i in the j-th subband at the ℓ-th decomposition level, and $|\mathfrak{W}(\mathcal{I}(i))|$ is the cardinality of the set $\mathfrak{W}(\mathcal{I}(i))$. The number 10^{-9} is used only for numerical convenience. In this paper, a neighborhood with size 3×3 for $\mathfrak{W}(\mathcal{I}(i))$ is used in the experiments.

4.4 Algorithm

By combining the results from the previous subsections, a fast adaptive iterative algorithm based on (23) for the optimization problem (16) is presented in Algorithm 1. The number of decomposition levels with the DHF is $J = 2$. The parameter κ is computed through (20). For a fixed $\alpha > 0$, we choose $\beta = \frac{1}{\alpha} - \frac{\kappa}{2} - 0.001$ that satisfies the first inequality in (24). The initial guess w^0 can be derived from the observed sum-of-squares (SoS) image u_{SoS}^g whose entry at the location $\mathbf{k}$ is defined as

$$u_{SoS}^g[\mathbf{k}] := \sqrt{\sum_{\ell=1}^{p} |g_\ell[\mathbf{k}]|^2}, \tag{26}$$

where g_ℓ is the ℓ-th coil image. It was known that the signal-to-noise ratio (SNR) in the SoS image is asymptotically (as the input SNR $\to \infty$) equal to that of maximum-ratio combining, which is the best unbiased reconstruction method when the coil sensitivities are known [26]. In other words, the image u_{SoS}^g is an approximation of the target image. Therefore, we choose $v^0 = w^0 = W u_{SoS}^g$.

Algorithm 1 (Fast Adaptive DHF Algorithm (FADHFA) for pMRI)

1. *Initialization: $v^0 = w^0 = W u_{sos}^g$ with g_{sos} given in (26); κ given in (20); the parameters $\alpha < \frac{2}{\kappa}$, $\beta = \frac{1}{\alpha} - \frac{\kappa}{2} - 0.001$, and non-negative θ satisfying (24);*

2. *For $k = 1, 2, \ldots$,*

   (a) *Estimate Γ via (25) only when k equals to 1, 6, 11, 16, 22 or 26;*

   (b) *compute (v^{k+1}, w^{k+1}) via (23);*

3. *Compute the image $u^{k+1} = W^\top v^{k+1}$ when a stopping condition is satisfied, then stop.*

Updating the regularization parameter matrix Γ in Algorithm 1 at $k = 1, 6, 11, 16, 22, 26$ is motivated by our numerical observations on the trend of the regularization parameters during the iterations. If we allow Γ to be estimated at each step, the values of estimated parameters at the first 50 steps for three randomly selected pixels are plotted in Figure 1. From this figure, we find that the values of these parameters tend to constants roughly after 25 iterations, we therefore propose in Algorithm 1 to update Γ only when k is 1, 6, 11, 16, 21 or 26. Finally, since the matrix Γ is fixed after the 26-th iteration, the convergence of Algorithm 1 is guaranteed by Theorem 2.
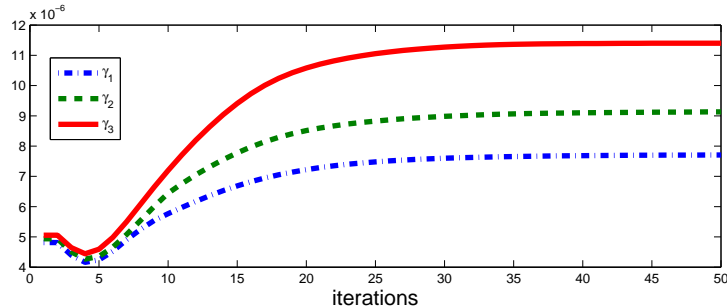
Figure 1: The values of three regularization parameters of Γ at the first 50 iterations.

5 Experiments

In this section, we illustrate the effectiveness of our model (15) and the corresponding algorithms in producing high-quality images from coil pseudo random downsampling k-space data in the phase-encoding direction on the Cartesian coordinate. Simulated test data is used in Section 5.1, phantom MR images acquired by an MRI machine are used in Section 5.2, and *in-vivo* medical MR coil images are used in Section 5.3.

To have a through comparison of the performance of the DHT for pMRI, we consider to replace our frame transform matrix W in FADHFA by two other wavelets. The first one is the three-level framelet transform using the tensor product complex tight framelet $\mathbb{C}\mathrm{TF}_6$ that has 6 filters and offers 14 directions in 2-dimension [19], and we will denote the resulting algorithm by FA$\mathbb{C}\mathrm{TF}_6$A. The excellent performance of $\mathbb{C}\mathrm{TF}_6$ in image denoising has been reported in a comparison with the dual tree complex wavelet transform and shearlets in [19]. The other is the two-level non-decimated wavelet transform using the orthogonal Haar wavelet from which we generated our directional Haar tight framelet system, and we will denote the corresponding algorithm by FAHaarA. We also compare our method with the TV-based regularization model (4) solved by the method in [46] and the method ℓ_1-ESPIRiT (an eigenvalue approach to autocalibrating parallel MRI) in [43]. The source code of the TV-based algorithm [46] was provided by the authors, and that of the ℓ_1-ESPIRiT method was downloaded from the web site of one of the authors[1]. We terminate our method when $\|u^{k+1} - u^k\|_2^2/\|u^k\|_2^2 < 10^{-8}$ or when the number of iterations exceeds 200. Here u^k is the kth iteration produced by the underlying algorithm. All experiments are performed in Matlab R2009a on a Lenovo X1 Carbon computer with Intel(R) Core(TM) i5-4200U processor (2.30GHz), 8G memory, and Windows 7 operating system.

5.1 Performance on Simulated Data

In this section, we compare the reconstruction performance of FADHFA against FA$\mathbb{C}\mathrm{TF}_6$A, FAHaarA, and the TV-based algorithm on the Shepp-Logan phantom of size 256-by-256 shown in Figure 2 (a). (It will be unfair for ℓ_1-ESPIRiT if we are to compare it with our method as it generates its own sensitivity profiles rather than using the true ones given below.)

The pixel values of the Shepp-Logan phantom range from 0 to 1. Assume that we have an array of 4 surface coils. The original phantom image is modulated by 4 different smoothly-decaying sensitivity

---

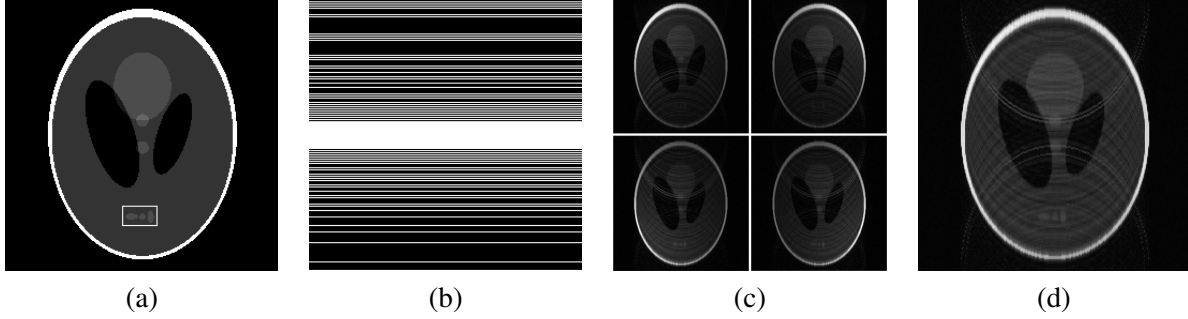[1]The code is available at: `http://www.eecs.berkeley.edu/~mlustig/Software.html`

Figure 2: (a) The Shepp-Logan phantom (the rectangle is for later zoom-in comparison); (b) Sampling model of the 33% k-space; (c) Four coil images with Gaussian noise $\sigma = 0.01$; (d) The SoS image from the 33% k-space.

profiles:

$$\mathcal{S}_1[i,j] = \zeta/(25000 + (i+40)^2 + (j+20)^2),$$
$$\mathcal{S}_2[i,j] = \zeta/(25000 + (i+50)^2 + (j-290)^2),$$
$$\mathcal{S}_3[i,j] = \zeta/(25000 + (i-290)^2 + (j+10)^2),$$
$$\mathcal{S}_4[i,j] = \zeta/(25000 + (i-280)^2 + (j-310)^2),$$

$i, j = 1, 2, \ldots, 256$ and the complex constant $\zeta = (25000 + \imath 25000)/\sqrt{2}$. For these sensitivity matrices, the parameter κ given in (20) is 1.012. More precisely, we perform an entry-wise multiplication of $\mathcal{S}_\ell$ with u, $\ell = 1, 2, 3, 4$, see (1). Then we apply the sampling model as in Figure 2 (b) for shortening imaging time in the k-space to obtain the noiseless coil images. We further add additive white Gaussian noise with noise level $\sigma = 0.01$ to each image to obtain the observed noisy coil images g_ℓ. The four noisy coil images from the phantom are shown in Figure 2 (c). The SoS image of four noisy coil images is shown in Figure 2 (d), which is obviously noisy and blurred with aliasing artifacts.

The result in Figure 3 (a) is obtained from solving the TV-based model (4). The regularization parameter λ in (4) is chosen to be 0.005 using trial and error for the best reconstruction quality. The results in Figure 3 (b), (c), and (d) are obtained by the FA$\mathbb{C}$TF$_6$A, FAHaarA, and FADHFA, respectively. We emphasize that FA$\mathbb{C}$TF$_6$A, and FAHaarA use the same model (16) except that the DHF tight frame system is replaced by $\mathbb{C}$TF$_6$ and the orthogonal Haar wavelet, respectively. Thus we used the same technique as given in Section 4.3 to estimate the regularization matrix for these methods. We can see that the aliasing artifacts and noise in Figure 2 (d) are significantly suppressed in Figures 3 (a)–(d).

For this test example, since the original phantom is available, we can measure the accuracy of the reconstructions by the normalized mean-squared error (NMSE), which is a global image quality metric that quantifies the difference between the ground true image u and the reconstruction $\hat{u}$. It is defined by

$$\text{NMSE} = \frac{\|u - \hat{u}\|_2^2}{\|u\|_2^2}.$$

A lower NMSE value means a better accuracy of reconstruction. In Table 1, the corresponding NMSE of the reconstructions in Figures 3 (a)–(d) are given. Clearly, the reconstruction given by FADHFA has the smallest NMSE value.

To further evaluate the quality of the images in Figures 3 (a)–(d), the zoom-in images of the region marked by the white rectangle in Figure 2 (a) are displayed in Figure 4. We observe that the edges in Figure 4 (c), (d), and (e), which are from the TV-based regularization, FA$\mathbb{C}$TF$_6$A, and FAHaarA, respectively, are
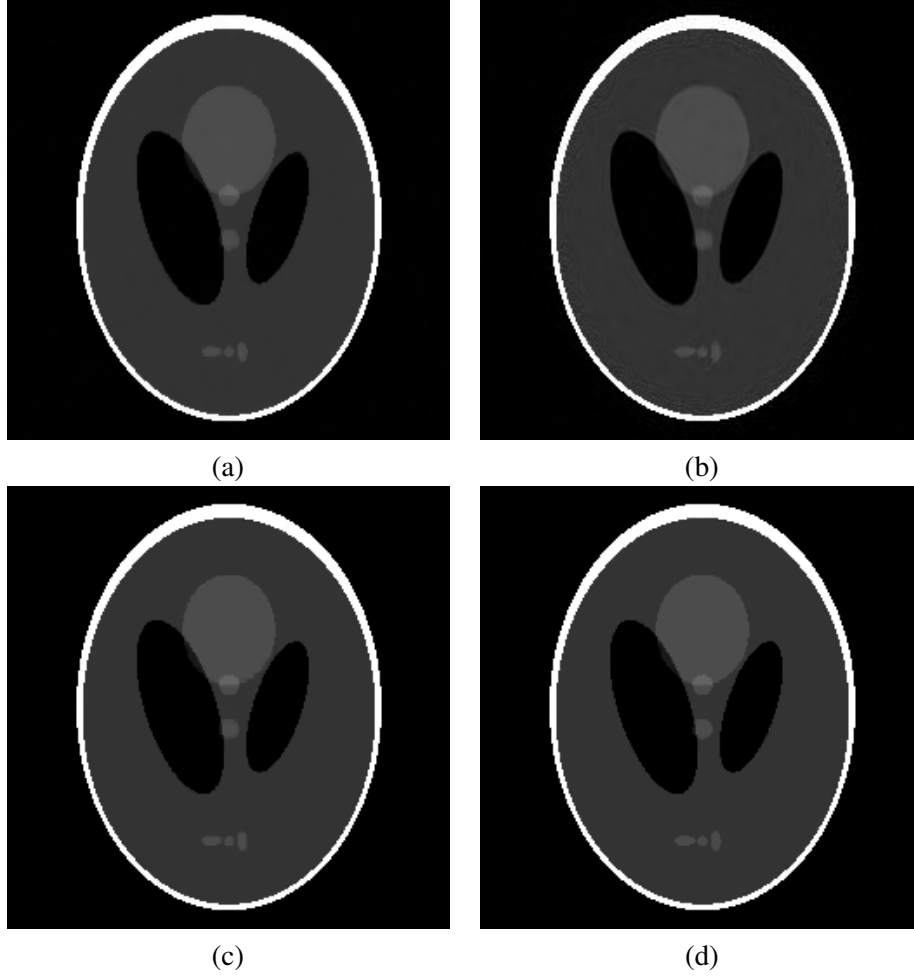
Figure 3: The reconstructed images by (a) the TV regularization algorithm [46] with parameter 0.005; (b) $FA\mathbb{C}TF_6A$; (c) FAHaarA; and (d) FADHFA, respectively.

blurry, while the edges in Figure 4 (f) by FADHFA are close to those in the original phantom shown in Figure 4 (a).

In Table 1 we also report the CPU time for obtaining the reconstructed images in Figure 3 (a)–(d). We see that our method requires the least time, and it is even faster than FAHaarA as explained at the end of Section 3. Since our tight algorithm FADHFA performs much better than $FA\mathbb{C}TF_6A$, and FAHaarA in terms of the quality of the reconstructed images and CPU time, we will not compare with these two methods in the following experiments.

Table 1: The NMSE indexes and the CPU usage for the reconstructions in Figure 3.

pMRI Algorithms	TV-based Alg. [46]	$FA\mathbb{C}TF_6A$	FAHaarA	FADHFA
NMSE	8.2×10^{-4}	2.6×10^{-3}	3.6×10^{-4}	2.19×10^{-4}
CPU Time	12.3s	48.2s	9.1s	9.0s

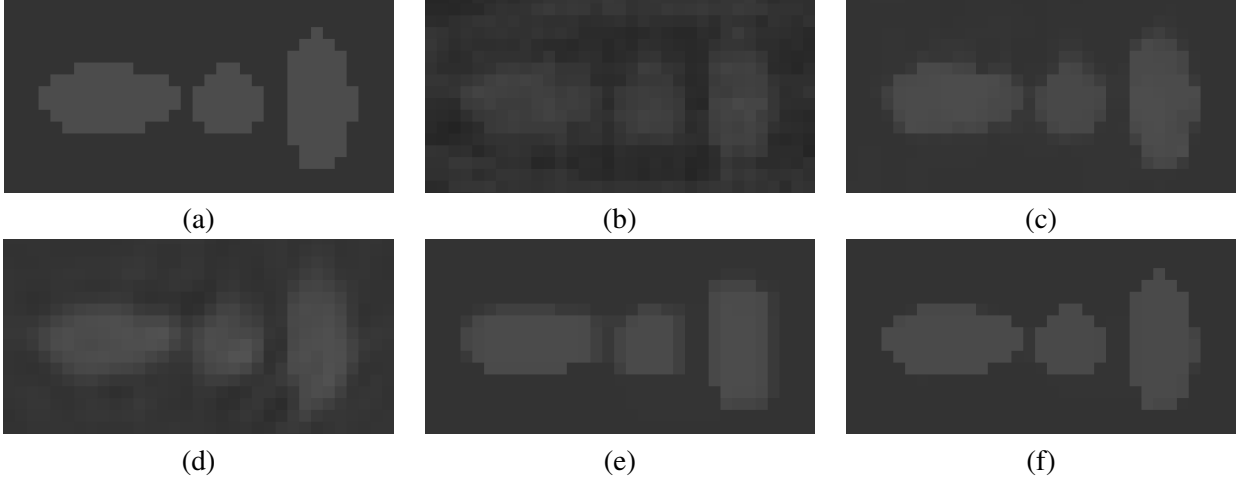|		
(a)	(b)	(c)
(d)	(e)	(f)

Figure 4: Zoom-in images of the region marked by the white rectangle in Figure 2(a). (a) Original phantom; (b) SoS image from the 33% k-space; the reconstructed images by (c) the TV regularization algorithm [46] with parameter 0.005; (d) FA$\mathbb{C}$TF$_6$A; (e) FAHaarA; and (f) FADHFA .

5.2 MRI Phantoms

In this subsection, phantom MR images are acquired on a 3T MRI System (Tim Trio, Siemens, Erlangen, Germany). A turbo spin-echo sequence was used to acquire T_2-weighted images. The detailed imaging parameters are as follows: field of view (FOV) = 256×256 mm^2, image marix size = 512×512, slice thicknesses (ST) = 3 mm, flip angle = 180 degree, repetition time (TR) = 4000 ms, echo time (TE) = 71 ms, echo train length (ETL) = 11 and number of excitation (NEX) = 1.

To accelerate the imaging speed, parts of each coil data are collected to fuse a desired image, which represent parts of the target imaging slice. An example with four coil images of size 512-by-512 is given here. According to the sampling model in Figure 5 (a), 33% of k-space data (marked by white color there) of each coil are collected for shortening imaging time. Figure 5 (b) is one of the coil images obtained by applying the inverse Fourier transform for the collected k-space data with zero-padding for missing data. Reconstructing the pMRI images from the observed coil images via problem (16) requires the availability of coil sensitivities. The approach of estimating the coil sensitivities proposed in [37, 4] roughly consists of two main steps: the first step is to identify a region of interpolation and the second step is to estimate the sensitivities through a polynomial locally fitting the pixels of the coil images on the interpolation region. In [37], the interpolation region was determined by checking whether the target signal in u^g_{SoS} given by (26) (see Figure 5 (c)) dominates noise or not.

To reduce the noise effects, we propose an alternative way to determine the interpolation region. Our method of estimating the coil sensitivities is described in the following. The observed SoS image u^g_{SoS} is first decomposed several levels by using the DHF filters. For the resulting coefficient matrices in the coarsest level, we component-wisely take the absolute values of the coefficient matrices and then add them up to a single coefficient matrix. From this resulting matrix and with a pre-given threshold, we generate a binary matrix whose entry is 1 (white) if this entry is above the threshold or 0 (black) otherwise. Figure 5 (d) is the resulting binary image. For this binary image, the value of 1 at a location indicates that the pixel values at that location in all the observed coil images g_ℓ can give feasible information of the target image. The collection of these locations then form the interpolation region. Given this region, the polynomial fitting procedure in [37][2] is used to obtain the sensitivity maps. Figure 5 (e) is the estimated coil sensitivity by

---

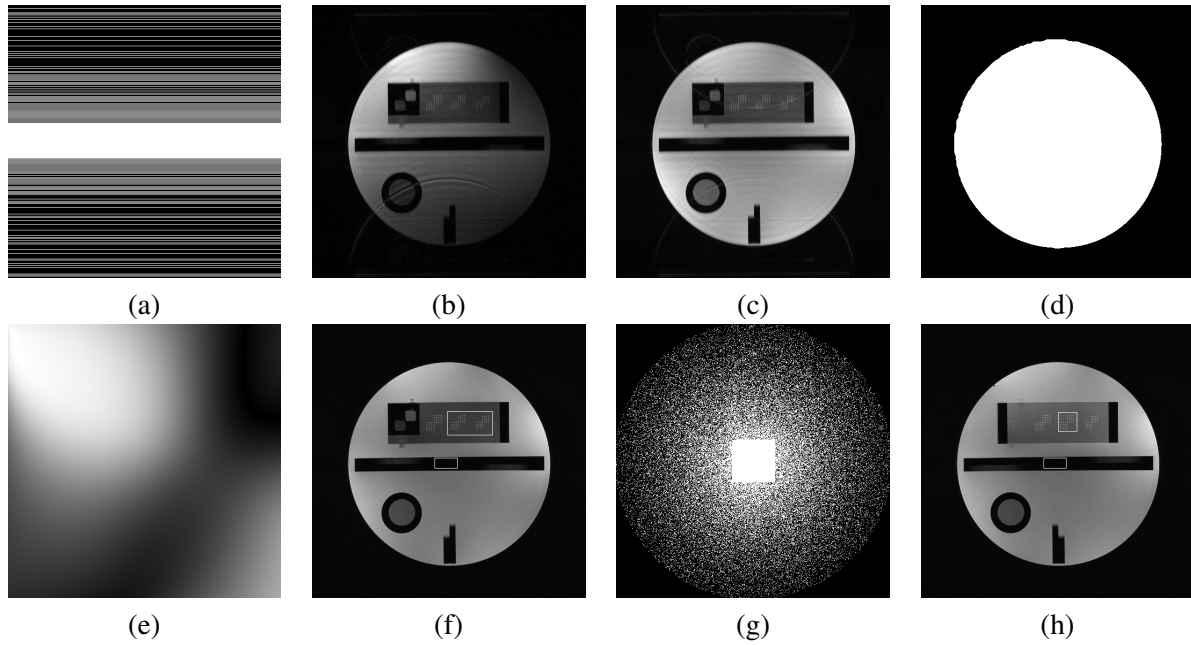[2]The code is available at: `http://maki.bme.ntu.edu.tw/?page_id=253`

Figure 5: (a) Sampling model of 33% k-space; (b) One coil image from the 33% k-space; (c) SoS image from the 33% k-space; (d) Binary image for the interpolation area of (c); and (e) Sensitivity estimated by fitting polynomial algorithm [37]; (f) SoS images of full k-space; (g) Sampling model of 25% k-space; and (h) SoS images of full k-space.
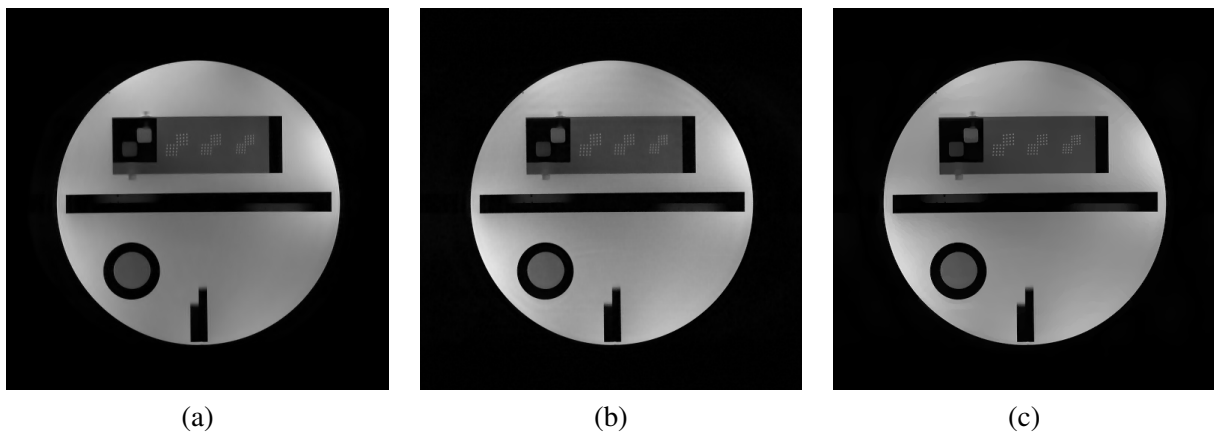

Figure 6: The reconstructed images from 33% k-space sample by (a) ℓ_1-ESPIRiT [43] with parameter 0.01; (b) TV regularization algorithm [46] with parameter 0.00013; and (c) Our FADHFA.

using the coil image data of Figure 5 (b) corresponding to the binary image of Figure 5 (d). With this scheme, each coil sensitivity can be efficiently estimated from parts of the k-space data.
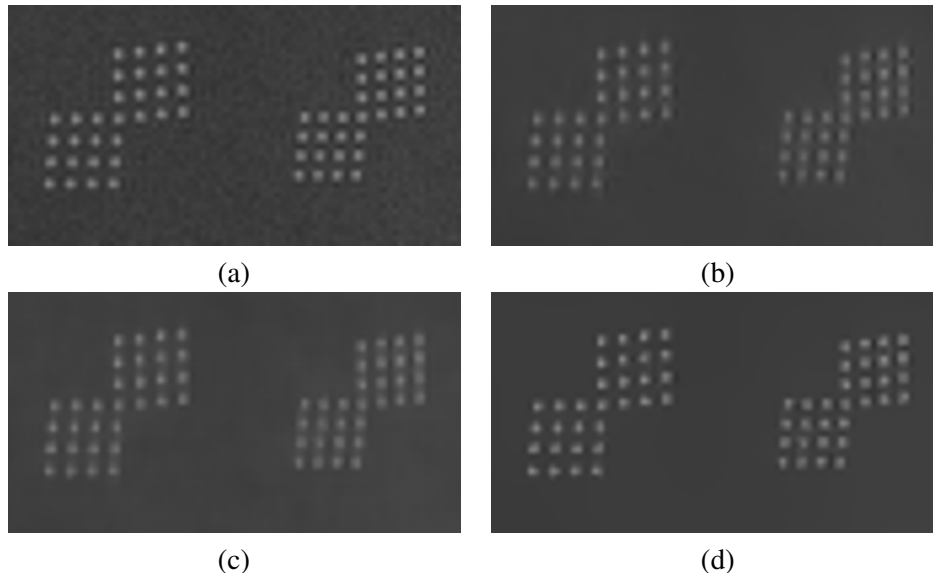

(a)

(b)

(c)

(d)

Figure 7: Zoom-in images of the region marked by a larger white rectangle in Figure 5. (a) SoS image of the full k-space in Figure 5 (f); the reconstructed images by (b) ℓ_1-ESPIRiT [43] with parameter 0.01; (c) TV regularization algorithm [46] with parameter 0.00013; and (d) Our FADHFA.
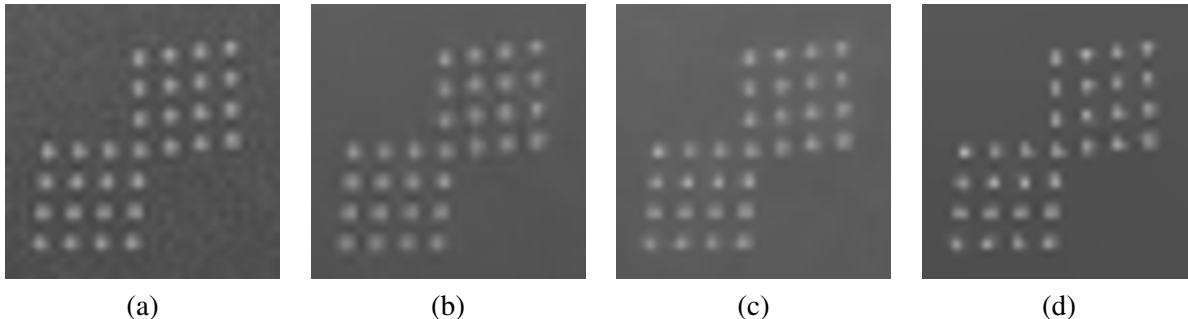

(a)

(b)

(c)

(d)

Figure 8: Performance of the results on another set of 4-coil images of Figure 5 (h) by 2-D pseudo random sampling model in Figure 5 (g). (a) SoS image of the full k-space with zoom-in part at the square region of Figure 5 (h); (b)–(d): ℓ_1-ESPIRiT [43] with parameter 0.008, TV regularization algorithm [46] with parameter 0.0001 and our FADHFA, respectively.

Three different approaches, namely, ℓ_1-ESPIRiT algorithm [43], total variation based reconstruction in [46], and our proposed FADHFA are used to reconstruct an image from four coil images with the sampling model described in Figure 5 (a).

The SoS image of the full k-space is considered as a reference image shown in Figure 5 (f). The image in Figure 6 (a) is the result from the ℓ_1-ESPIRiT using the default settings in the source code of ℓ_1-ESPIRiT algorithm [43] except that the regularization parameter is set to be 0.01 after an extensive trail-and-error search to find the best one. The reconstructed image via (4) by the method in [46] is displayed in Figure 6 (b). The reconstructed image by the FADHFA is shown in Figure 6 (c). Clearly, aliasing artifacts appeared in Figure 5 (c) are significantly suppressed by the three methods.

Table 2: First number in parentheses: the CNR values for the regions marked in Figure 5 (f) (i.e. Figure 7) and Figure 5 (h) (i.e. Figure 8). Second number in parentheses: the CPU time in seconds for the reconstructions of the whole image by the various algorithms.

% of k-space	Zoom-in image	ℓ_1-ESPIRiT [43]	TV-based Alg. [46]	Our FADHFA
33%	Figure 7	(65.0, 255s)	(73.3, 65s)	(124.4, 28s)
25%	Figure 8	(91.0, 256s)	(108.0, 67s)	(168.1, 44s)

To further evaluate the quality of the reconstructions, we zoom in to the region containing the bright dots given in Figure 5 (f). They are depicted as Figure 7 (a)–(d), respectively. We can see that the image in Figure 7 (a) is more noisy than the other images in Figure 7. The dots in Figure 7 (d) are sharper and brighter than those in Figure 7 (b) and (c), which are close to dots by SoS image of the full k-space in Figure 7 (a). We conclude that our FADHFA performs better in preserving the details of the images and removing noisy artifacts in smooth area. Furthermore, unlike the TV-based method or the ℓ_1-ESPIRiT method, our proposed FADHFA automatically updates the regularization parameters.

Since we do not know the ground true phantom, the CNR (contrast-to-noise ratio) is utilized to measure the quality of the reconstructed images quantitatively. The CNR index is a local quality metric and is defined as the ratio of a target region contrast to the background noise as

$$\text{CNR} = \frac{|\mathbb{E}_{\Omega_T}(\hat{u}) - \mathbb{E}_{\Omega_B}(\hat{u})|}{\sigma_{\Omega_B}(\hat{u})},$$

where $\hat{u}$ is an reconstructed image. Here, $\mathbb{E}_{\Omega_T}$ is the mean of a specific bright target region Ω_T, $\mathbb{E}_{\Omega_B}$ is the mean of an uniform region Ω_B (darkness), and σ_{Ω_B} is the standard deviation over the region Ω_B. Higher CNR implies better ability to detect the lesion by an observer [25, 40]. We use the big rectangle in Figure 5 (f) as the bright target region Ω_T and the small rectangle in the middle as the uniform region Ω_B to evaluate the CNR values for the images in Figures 6 (b)–(d).

The CNR values by ℓ_1-ESPIRiT [43], TV-based algorithm [46] and our FADHFA are given in Table 2. Our FADHFA gives the highest CNR value, which means that it allows one to better detect lesions in the reconstructed images. The CPU times by ℓ_1-ESPIRiT [43], TV-based algorithm [46] and our FADHFA are also given there which show that our FADHFA is fastest in reconstructing the MRI image. We emphasize here again we only have to solve our problem once as we do not have to estimate the regularization parameter, while the other methods may have to solve the corresponding problems several times to get the best regularization parameters.

The FADHFA, the ℓ_1-ESPIRiT [43] and TV-based regularization method are applied to another 4-coil images by 2-D pseudo random sampling model. The sampling model given in Figure 5 (g) is used to collect a 25% k-space data. Figure 5 (h) is the reference SoS image of full k-space data. The regularization parameters in (4) and in ℓ_1-ESPIRiT are set to be 0.0001 and 0.008, respectively by trial-and-error. To compare the reconstructed images conveniently, we just present the region marked by the square in Figure 5 (h). The zoomed-in region of reference SoS image of full k-space data is displayed in Figure 8 (a). The corresponding results by ℓ_1-ESPIRiT, the TV-based regularization method and FADHFA are shown in Figures 8 (b), (c), and (d), respectively. Again, we can conclude that FADHFA performs better than the TV-based regularization method in terms of preserving the edges and removing the artifacts. To calculate the CNR values in this test, the square and rectangular regions in Figure 5 (h) are identified as the bright target region Ω_T and background uniform region Ω_B, respectively. The CNR values and CPU times of ℓ_1-ESPIRiT [43], TV-based algorithm [46] and our FADHFA are given in Table 2. It shows that our FADHFA gives the highest CNR value and needs the least CPU times. Unlike the TV-based method and ℓ_1-ESPIRiT, our FADHFA does not need to set the regularization parameters by hand. That makes it more suitable for real clinical applications on different slices and sampling models.
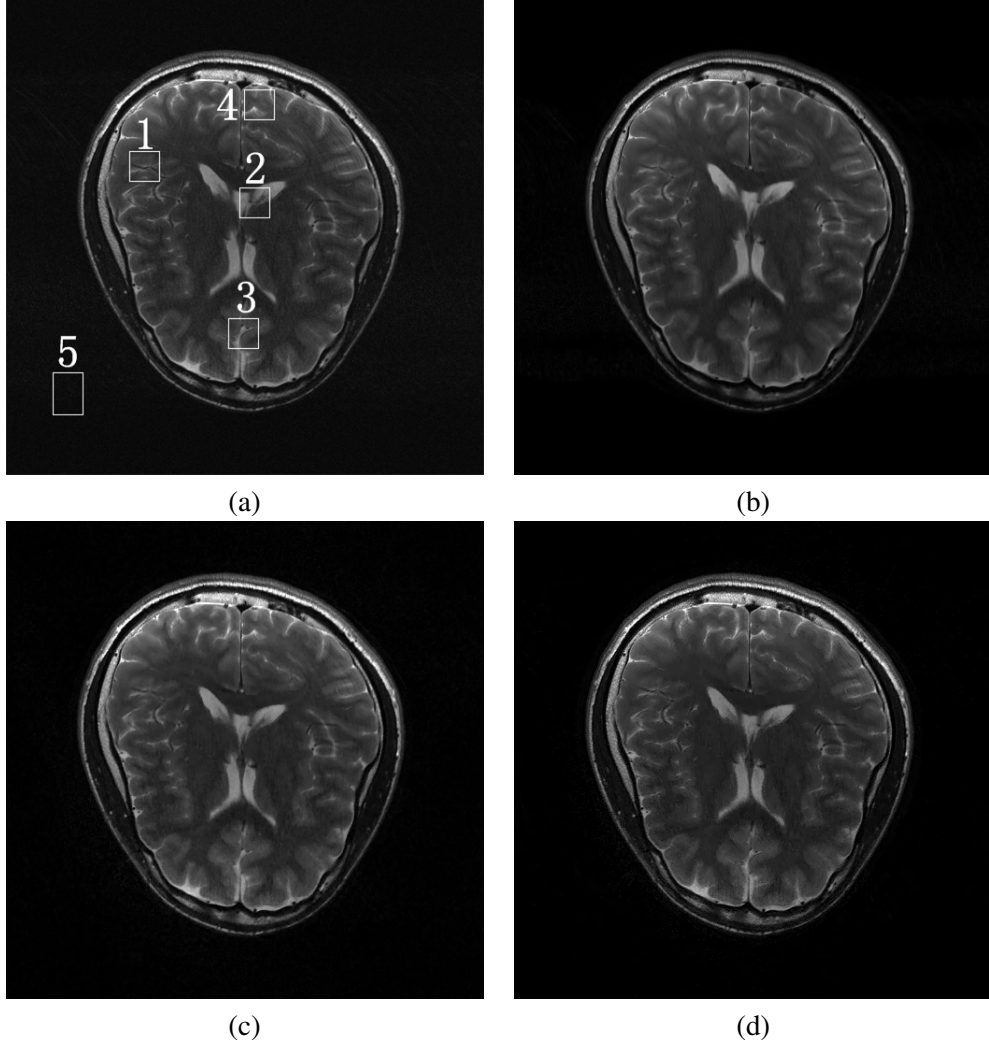
Figure 9: (a) SoS image of the full k-space with zoom-in parts. (b) ℓ_1-ESPIRiT [43] with parameter 0.006. (c) TV regularization algorithm [46] with parameter 0.00015. (d) Our FADHFA.

5.3 In-vivo Data

In this subsection we test our DHF-based algorithm FADHFA on MRI data that are obtained by head examination from a healthy volunteer. The imaging was done on a 3T MRI system (Tim Trio, Siemens, Erlangen, Germany). A turbo spin-echo sequence was used to acquire transverse T_2-weighted images. The detailed imaging parameters are as follows: field of view (FOV) = 256×256 mm^2, image marix size = 512×512, slice thicknesses (ST) = 3.5 mm, flip angle = 180 degree, repetition time (TR) = 4000 ms, echo time (TE) = 94 ms, echo train length (ETL) = 11 and number of excitation (NEX) = 1.

For the 12-coil images of a slice, the SoS image of the full k-space details is shown in Figure 9 (a). Then 33% full k-space data are sampled using the sampling model that is the same as the one in Figure 5 (a). Figures 9 (b), (c) and (d) show the reconstructions from the 33% full k-space data by the ℓ_1-ESPIRiT, TV-based and FADHFA algorithms, respectively. The regularization parameter in (4) is set to be 0.00015, and the regularization parameter of ℓ_1-ESPIRiT [43] is set to be 0.006.

In Table 3, the CPU time by ℓ_1-ESPIRiT [43], TV-based algorithm [46] and our FADHFA are given. Our FADHFA only costs about one sixth of the CPU time used by ℓ_1-ESPIRiT [43] and is twice faster than

Table 3: The CNR values at four different square regions marked in Figure 9 (a) and CPU time (in seconds) by pMRI algorithms.

pMRI Algorithms	Region **1**	Region **2**	Region **3**	Region **4**	Times
ℓ_1-ESPIRiT [43]	39.21	45.19	34.61	40.39	293s
TV-based Alg. [46]	59.03	68.82	66.99	84.51	108s
Our FADHFA	192.17	223.06	217.45	272.70	50s

(a)   (b)   (c)   (d)

(e)   (f)   (g)   (h)

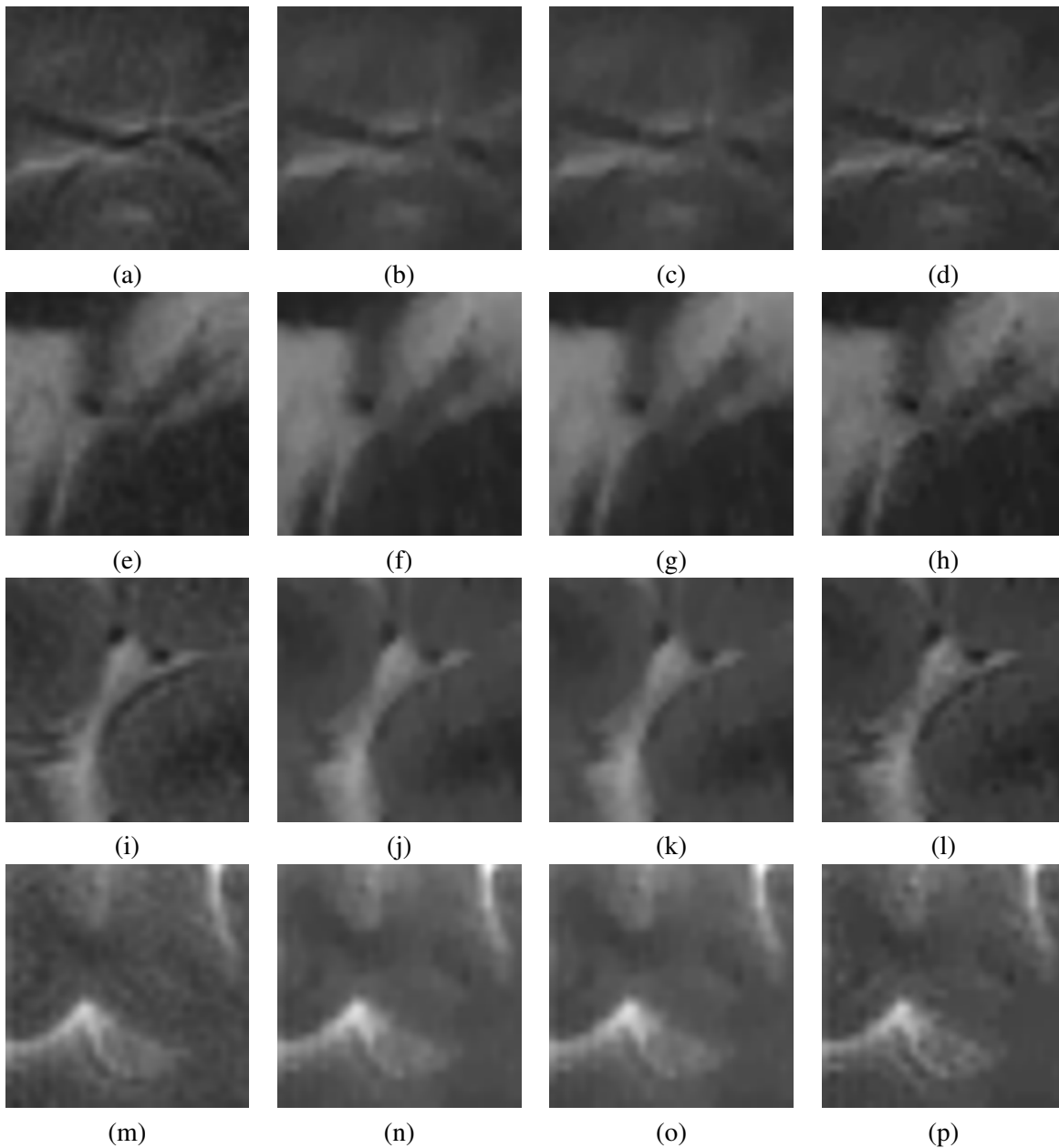(i)   (j)   (k)   (l)

(m)   (n)   (o)   (p)

Figure 10: Zoom-in parts of the square regions **1**, **2**, **3** and **4** in Figure 9 (a). The first column: Reference SoS image of the full k-space. The reconstructed images of the second, third and forth columns by ℓ_1-ESPIRiT [43], TV regularization algorithm [46] and our FADHFA on 33% full k-space data, respectively.

the TV-based algorithm [46]. To compare the quality of the reconstructions by ℓ_1-ESPIRiT, the TV-based algorithm and FADHFA in terms of the CNR values, in Figure 9 (a), the regions marked by the squares are respectively considered as the bright target region Ω_T and the one by the rectangle labeled by 5 as background uniform region Ω_B. For example, at square region 1, the CNR values by ℓ_1-ESPIRiT [43], TV-based algorithm [46] and our FADHFA are 39.21, 59.03 and 192.17, respectively. The CNR value by FADHFA is about five and three times higher than that by ℓ_1-ESPIRiT [43] and by TV-based algorithm [46], respectively. We can see that our FADHFA always provides the highest CNR value for each region in Table 3, and therefore, FADHFA always gives good contrast results for detecting lesions.

To conveniently distinguish the difference of the reconstructed images, we zoom-in region 1 marked in Figure 9 (a), and provide the zoom-in images in Figures 10 (a)–(d) corresponding to the images displayed in Figures 9 (a)–(d). Clearly, the quality of the images in Figures 10 (d) is much better than the one in Figure 10 (c) in terms of the sharpness of the brain tissue. The boundary of the organ tissue in Figure 10 (d) is more obvious than that in Figure 10 (c). This indicates that our directional Haar wavelet-based regularization term is better than TV regularization to preserve details of the structures and to suppress the noise. Meanwhile, the detail structures in Figure 10 (d) by FADHFA is more noticeable than that in Figure 10 (b) by ℓ_1-ESPIRiT, which is closer to the reference SoS image of the full k-space in Figure 10 (a) and makes the difference of organ structures to be distinguished easily.

The zoom-in regions 2, 3 and 4 marked in Figure 9 (a) are provided in the second, third and forth rows of Figure 10, respectively. The contrast in Figure 10 (h) by FADHFA is more noticeable to distinguish the difference of organ than that in Figure 10 (g) by ℓ_1-ESPIRiT and that in Figure 10 (f) by TV-based algorithm. For region 3, our FADHFA is still better to preserve the details of tissue structures than ℓ_1-ESPIRiT and TV-based algorithm. The boundary of different tissues in Figure 10 (l) by FADHFA is clearer than that in Figure 10 (j) by ℓ_1-ESPIRiT and that in Figure 10 (k) by TV-based algorithm. For region 4, Figure 10 (p) by FADHFA is much closer to reference image in Figure 10 (m) than Figure 10 (n) by ℓ_1-ESPIRiT and that in Figure 10 (o) by TV-based algorithm. All these observations are consistent with the CNR values presented in Table 3, which again confirm that the proposed fast DHF-based pMRI reconstruction algorithm FADHFA is robust against the noise on different MRI machines with different coil receivers.

6   Conclusions

We constructed a directional Haar framelet (DHF) system whose filters have the ability to capture information of edges of images in the horizonal, vertical, and $\pm 45^o$ directions. The computational complexity of the fast tight frame transform with DHT is lower than that with the orthogonal Haar wavelet transform. We proposed a pMRI reconstructed model in real domain whose regularization term was formed from the DHF. The reconstruction model can be efficiently solved by a proximal algorithm. We developed a way to automatically update the regularization parameter in each iteration of the algorithm. Finally, the performance of the proposed model was demonstrated for in-silico and in-vivo data sets.

References

[1] M. BLAIMER, F. BREUER, M. MUELLER, R. M. HEIDEMANN, M. A. GRISWOLD, AND P. M. JAKOB, *SMASH, SENSE, PILS, GRAPPA: how to choose the optimal method*, Topics in Magnetic Resonance Imaging, 15 (2004), pp. 223–236.

[2] K. T. BLOCK, M. UECKER, AND J. FRAHM, *Undersampled radial MRI with multiple coils. iterative image reconstruction using a total variation constraint*, Magnetic Resonance in Medicine, 57 (2007), pp. 1086–1098.

[3] K. BREDIES, K. KUNISCH, AND T. POCK, *Total generalized variation*, SIAM Journal on Imaging Sciences, 3 (2010), pp. 492–526.

[4] M. BYDDER, D. LARKMAN, AND J. HAJNAL, *Combination of signals from array coils using image-based estimation of coil sensitivity profiles*, Magnetic Resonance in Medicine, 47 (2002), pp. 539–548.

[5] J. F. CAI, R. H. CHAN, AND Z. SHEN, *A framelet-based image inpainting algorithm*, Applied and Computational Harmonic Analysis, 24 (2008), pp. 131–149.

[6] J.-F. CAI, B. DONG, S. OSHER, AND Z. SHEN, *Image restorations: total variation, wavelet frames and beyond*, Journal of the American Mathematical Society, 25 (2012), pp. 1033–1089.

[7] J.-F. CAI, B. DONG, AND Z. SHEN, *Image restorations: A wavelet frame based model for piecewise smooth functions and beyond*, Applied and Computational Harmonic Analysis, accepted, (2015).

[8] L. CHAâRI, J. C. PESQUET, A. BENAZZA-BENYAHIA, AND P. CIUCIU, *A wavelet-based regularized reconstruction algorithm for SENSE parallel MRI with applications to neuroimaging*, Medical Image Analysis, 12 (2011), pp. 185–201.

[9] R. H. CHAN, T. F. CHAN, L. SHEN, AND Z. SHEN, *Wavelet algorithms for high-resolution image reconstruction*, SIAM Journal on Scientific Computing, 24 (2003), pp. 1408–1432.

[10] ——, *Wavelet deblurring algorithms for spatially sarying blur from high-resolution image reconstruction*, Linear Algebra and Applications, 366 (2003), pp. 139–155.

[11] R. H. CHAN, S. D. RIEMENSCHNEIDER, L. SHEN, AND Z. SHEN, *High-resolution image reconstruction with displacement errors: a framelet approach*, International Journal of Imaging Systems and Technology, 14 (2004), pp. 91–104.

[12] R. H. CHAN, S. D. RIEMENSCHNEIDER, L. SHEN, AND Z. SHEN, *Tight frame: an efficient way for high-resolution image reconstruction*, Applied and Computational Harmonic Analysis, 17 (2004), pp. 91–115.

[13] T. CHAN, S. ESEDOGLU, AND F. PARK, *Image decomposition combining staircase reduction and texture extraction*, Journal of Visual Communication and Image Representation, 18 (2007), pp. 464–486.

[14] A. DESHMANE, V. GULANI, M. A. GRISWOLD, AND N. SEIBERLICH, *Parallel MR imaging*, Journal of Magnetic Resonance Imaging, 36 (2012), pp. 55–72.

[15] J. A. FESSLER, *Model-based image reconstruction for MRI*, IEEE Signal Processing Magazine, 27 (2010), pp. 81–89.

[16] M. A. GRISWOLD, F. BREUER, M. BLAIMER, S. KANNENGIESSER, R. HEIDEMANN, M. MUELLER, M. NITTKA, V. JELLUS, B. KIEFER, AND P. M. JAKOB, *Autocalibrated coil sensitivity estimation for parallel imaging*, NMR in Biomedicine, 19 (2006), pp. 316–324.

[17] M. A. GRISWOLD, P. M. JAKOB, AND Q. CHEN, *Resolution enhancement in single-shot imaging using simultaneous acquisition of spatial harmonics (SMASH)*, Magnetic Resonance in Medicine, 41 (1999), pp. 1236–1245.

[18] M. A. GRISWOLD, P. M. JAKOB, R. M. HEIDEMANN, M. NITTKA, V. JELLUS, J. WANG, B. KIEFER, AND A. HAASE, *Generalized autocalibrating partially parallel acquisitions (GRAPPA)*, Magnetic Resonance in Medicine, 47 (2002), pp. 1202–1210.

[19] B. HAN AND Z. ZHAO, *Tensor product complex tight framelets with increasing directionality*, SIAM Journal on Imaging Sciences, 7 (2014), pp. 997–1034.

[20] R. HORN AND C.JOHNSON, *Topics in matrix analysis*, Cambridge University Press, 1991.

[21] A. HYVARINEN, *Sparse code shrinkage: Denoising of non-gaussian data by maximum likelihood estimation*, Neural Computation, 11 (1999), pp. 1739–1768.

[22] J. IMMWEKÆR, *Fast noise variance estimation*, Computer Vision and Image Understanding, 64 (1996), pp. 300–302.

[23] S. L. KEELING, C. CLASON, M. HINTERMLLER, F. KNOLL, A. LAURAIN, AND G. VON WINCKEL, *An image space approach to Cartesian based parallel MR imaging with total variation regularization*, Medical Image Analysis, 16 (2012), pp. 189–200.

[24] F. KNOLL, C. CLASON, K. BREDIES, M. UECKER, AND R. STOLLBERGER, *Parallel imaging with nonlinear reconstruction using variational penalties*, Magnetic Resonance in Medicine, 67 (2012), pp. 34–41.

[25] A. KROL, S. LI, L. SHEN, AND Y. XU, *Preconditioned alternating projection algorithms for maximum a posteriori ECT reconstruction*, Inverse Problems, 28 (2012), p. 115005.

[26] E. G. LARSSON, D. ERDOGMUS, R. YAN, J. C. PRINCIPE, AND J. R. FITZSIMMONS, *SNR-optimality of sum-of-squares reconstruction for phased-array magnetic resonance imaging*, Journal of Magnetic Resonance, 163 (2003), pp. 121–123.

[27] Q. LI AND N. ZHANG, *Fast proximity-gradient algorithms for structured convex optimization problems*, Applied and Computational Harmonic Analysis, accepted.

[28] Y. R. LI, D. Q. DAI, AND L. SHEN, *Multiframe super-resolution reconstruction using sparse directional regularization*, IEEE Transactions on Circuits and Systems for Video Technology, 20 (2010), pp. 945–956.

[29] Y. R. LI, L. SHEN, D. Q. DAI, AND B. W. SUTER, *Framelet algorithms for de-blurring images corrupted by impulse plus Gaussian noise*, IEEE Transactions on Image Processing, 20 (2011), pp. 1822–1837.

[30] Y. R. LI, L. SHEN, AND B. W. SUTER, *Adaptive inpainting algorithm based on DCT induced wavelet regularization*, IEEE Transactions on Image Processing, 22 (2013), pp. 752–763.

[31] F.-H. LIN, K. K. KWONG, J. W. BELLIVEAU, AND L. L. WALD, *Parallel imaging reconstruction using automatic regularization*, Magnetic Resonance in Medicine, 51 (2004), pp. 559–567.

[32] B. LIU, K. KING, M. STECKNER, J. XIE, J. SHENG, AND L. YING, *Regularized sensitivity encoding (SENSE) reconstruction using Bregman iterations*, Magnetic Resonance in Medicine, 61 (2009), pp. 145–152.

[33] M. LUSTIG, D. DONOHO, AND J. M. PAULY, *Sparse MRI: The application of compressed sensing for rapid MR imaging*, Magnetic Resonance in Medicine, 58 (2007), pp. 1182–1195.

[34] M. MURPHY, M. ALLEY, J. DEMMEL, K. KEUTZER, S. VASANAWALA, AND M. LUSTIG, *Fast ℓ_1-SPIRiT compressed sensing parallel imaging MRI: Scalable parallel implementation and clinically feasible runtime*, IEEE Transactions on Medical Imaging, 31 (2012), pp. 1250–1262.

[35] R. A. NOVELLINE AND L. F. SQUIRE, *Squire's fundamentals of radiology*, 5th Edition, Cambridge: Harvard University Press, 1997.

[36] S. PARK AND J. PARK, *Adaptive self-calibrating iterative GRAPPA reconstruction*, Magnetic Resonance in Medicine, 67 (2012), pp. 1721–1729.

[37] K. P. PRUESSMANN, M. WEIGER, M. B. SCHEIDEGGER, AND P. BOESIGER, *SENSE: sensitivity encoding for fast MRI*, Magnetic Resonance in Medicine, 42 (1999), pp. 952–962.

[38] S. RAVISHANKAR AND Y. BRESLER, *MR image reconstruction from highly undersampled k-space data by dictionary learning*, IEEE Transactions on Medical Imaging, 30 (2011), pp. 1028–1041.

[39] L. SHEN, M. PAPADAKIS, I. A. KAKADIARIS, I. KONSTANTINIDIS, D. KOURI, AND D. HOFFMAN, *Image denoising using a tight frame*, IEEE Transactions on Image Processing, 15 (2006), pp. 1254–1263.

[40] J. SIJBERS, P. SCHEUNDERS, N. BONNET, D. V. DYCK, AND E. RAMAN, *Quantification and improvement of the signal-to-noise ratio in a magnetic resonance image acquisition procedure*, Magnetic Resonance Imaging, 14 (1996), pp. 1157–1163.

[41] G. STRANG AND T. Q. NGUYEN, *Wavelets and Filterbanks*, Wellesley, MA: Wellesley-Cambridge, 1997.

[42] P. THUNBERG AND P. ZETTERBERG, *Noise distribution in SENSE- and GRAPPA-reconstructed images: a computer simulation study*, Magnetic Resonance Imaging, 25 (2007), pp. 1089–1094.

[43] M. UECKER, P. LAI, M. J. MURPHY, P. VIRTUE, M. ELAD, J. M. PAULY, S. S. VASANAWALA, AND M. LUSTIG, *ESPIRiT†an eigenvalue approach to autocalibrating parallel MRI: where SENSE meets GRAPPA*, Magnetic Resonance in Medicine, 71 (2014), pp. 990–1001.

[44] M. WEIGER, K. P. PRUESSMANN, AND P. BOESIGER, *Cardiac real-time imaging using SENSE*, Magnetic Resonance in Medicine, 43 (2000), pp. 177–184.

[45] D. S. WELLER, J. R. POLIMENI, L. GRADY, L. L. WALD, E. ADALSTEINSSON, AND V. K. GOYAL, *Sparsity-promoting calibration for GRAPPA accelerated parallel MRI reconstruction*, IEEE Transactions on Medical Imaging, 32 (2013), pp. 1325–1335.

[46] X. YE, Y. CHEN, AND F. HUANG, *Computational acceleration for mr image reconstruction in partially parallel imaging*, IEEE Transactions on Medical Imaging, 30 (2011), pp. 1055–1063.

[47] L. YING AND J. SHENG, *Joint image reconstruction and sensitivity estimation in SENSE (JSENSE)*, Magnetic Resonance in Medicine, 57 (2007), pp. 1196–1202.

[48] L. YUAN, L. YING, D. XU, AND Z.-P. LIANG, *Truncation effects in SENSE reconstruction*, Magnetic Resonance Imaging, 24 (2006), pp. 1311–1318.

[49] B. ZHAO, H. GAO, H. DING, AND S. MOLLOI, *Tight-frame based iterative image reconstruction for spectral breast CT*, Medical Physics, 40 (2013), p. 031905.

[50] T. ZHAO AND X. HU, *Iterative GRAPPA (iGRAPPA) for improved parallel imaging reconstruction*, Magnetic Resonance in Medicine, 59 (2008), pp. 903–907.